11066

1.0
1.1
1.25

4.5
5.6

2.8
3.2
3.6
4.0

2.5
2.2
2.0
1.8

1.4

1.6

MICROCOPY RESOLUTION TEST CHART
NATIONAL BUREAU OF STANDARDS 1963-A

AD A110664

LEVEL II (12)

BOUNDARY LAYER AND SIDE FORCE CHARACTERISTICS
OF NON-SPINNING AND SPINNING
AXISYMMETRIC BODIES

Thomas J. Mueller, Robert C. Nelson,

Jerome T. Kegelman and Robert J. Zehentner

DTIC
SELECTED
FEB 0 9 1982
E

UNIVERSITY OF NOTRE DAME

NOTRE DAME, INDIANA

for

U. S. ARMY RESEARCH OFFICE

UNIVERSITY OF NOTRE DAME, NOTRE DAME, IN 46556

DEPARTMENT OF AEROSPACE
AND MECHANICAL ENGINEERING

REPORT DOCUMENTATION PAGE		READ INSTRUCTIONS BEFORE COMPLETING FORM
1. REPORT NUMBER UNDAS-TN-127	2. GOVT ACCESSION NO. AD-A110 664	3. RECIPIENT'S CATALOG NUMBER
4. TITLE (and Subtitle) Boundary Layer Visualization and Side Force Characteristics of Non-Spinning and Spinning Axisymmetric Bodies		5. TYPE OF REPORT & PERIOD COVERED Final June 1978 – September 1981
		6. PERFORMING ORG. REPORT NUMBER
7. AUTHOR(s) Thomas J. Mueller, Robert C. Nelson, Jerome T. Kegelman and Robert J. Zehentner		8. CONTRACT OR GRANT NUMBER(s) DAAG29-78-G-0102 DAAG29-80-C-0127
9. PERFORMING ORGANIZATION NAME AND ADDRESS Dept. of Aerospace and Mechanical Engineering University of Notre Dame Notre Dame, IN 46556.		10. PROGRAM ELEMENT, PROJECT, TASK AREA & WORK UNIT NUMBERS DRXRO-PR P-15336-E
11. CONTROLLING OFFICE NAME AND ADDRESS U.S. Army Research Office P.O. Box 12211 Research Triangle Park, NC 27709.		12. REPORT DATE November 1981
		13. NUMBER OF PAGES 89
14. MONITORING AGENCY NAME & ADDRESS(if different from Controlling Office)		15. SECURITY CLASS. (of this report) UNCLASSIFIED
		16a. DECLASSIFICATION/DOWNGRADING SCHEDULE

16. DISTRIBUTION STATEMENT (of this Report)

Approved for public release: distribution unlimited.

17. DISTRIBUTION STATEMENT (of the abstract entered in Block 20, if different from Report)

18. SUPPLEMENTARY NOTES

19. KEY WORDS (Continue on reverse side if necessary and identify by block number)

Boundary Layer Transition
Cross-Flow Vortices
Smoke Flow Visualization
Axisymmetric Bodies

20. ABSTRACT (Continue on reverse side if necessary and identify by block number)

The results of an experimental investigation of the influence of spin and nose bluntness on the boundary layer characteristics and side force of a secant ogive nose axisymmetric body are presented. Smoke visualization data for the sharp and 10%, 20% and 30% spherically blunted noses were correlated with side forces measured at Reynolds numbers of 315,000 and 1,030,000, and spin rates up to 6000 rpm for angles of attack from 0° to 10°. Boundary layer flow asymmetries were correlated with the side forces measured to provide some insight into the origin of the side forces.

DD FORM 1473 EDITION OF 1 NOV 65 IS OBSOLETE
1 JAN 73

PREFACE

Accession For	
NTIS GRA&I	X
DTIC TAB	
Unannounced	
Justification	
By	
Distribution/	
Availability Codes	
Dist	Avail and/or Special
A	

DTIC
COPY
INSPECTED

iii

TABLE OF CONTENTS

LIST OF ILLUSTRATIONS

LIST OF ILLUSTRATIONS (Cont.)

LIST OF ILLUSTRATIONS (Cont.)

LIST OF ILLUSTRATIONS (Cont.)

LIST OF ILLUSTRATIONS (Cont.)

INTRODUCTION

General Remarks

The flight dynamics of a spinning body of revolution can be significantly influenced by the Magnus forces and moments acting on the body. These forces and moments are major contributors to the dispersion of spin stabilized projectiles and are the dominant mechanisms which produce flight instabilities. Previous investigations have shown the Magnus force to be a function of Reynolds number, Mach number, ratio of peripheral to free stream velocity, angle of attack and body geometry. The side force acting on axisymmetric spinning bodies is more complicated than the well-known *Magnus effect on a spinning two-dimensional circular cylinder.* This is due to the three-dimensional nature of the flow over a spinning axisymmetric body at angle of attack.

Some progress has been made in the past ten years concerning the theoretical,[1-5] experimental,[5-14] and numerical[15-17] aspects of the Magnus problem. Furthermore, this time period has seen a major shift towards numerical studies of this problem. As computational methods and computing equipment improve, these approximate numerical solutions of the complex three-dimensional flows over spinning bodies will become more practical and more nearly exact. It is well known that the separated and transitional flows which occur in actual flight situations have strong influences on the Magnus forces. It is also well known that, while our physical understanding of these complex flows is somewhat better than a decade ago, it is still not sufficient to support future numerical efforts.

Since the Magnus force originates in the boundary layer, it is directly related to the boundary layer characteristics, e.g., whether the boundary layer is predominantly laminar or turbulent.[7] Although there are significant differences between compressible and incompressible boundary layer flows, physical notions of fundamental importance may be obtained by studying incompressible flows. For example, the mechanisms of transition and turbulence production in the boundary layer are not affected by compressibility.[18] In addition, visual and hot-wire anemometer studies at low speed allow a detailed examination of the transition and separation processes not available in compressible high speed experiments. Therefore, the detailed results and

subsequent understanding obtained at low speeds will also be useful in high speed situations. To continue developing an accurate analytical and/or numerical method to predict the Magnus characteristics, one needs to accumulate a data base and improve our physical understanding concerning the effects of spin and body shape on the pertinent boundary layer characteristics. This was the primary objective of this research effort.

Description of the Problem

The transition process in the boundary layer of an axisymmetric body is the keystone which determines the magnitude and direction of the aerodynamic forces acting on the body. These forces are closely related to how rapidly the boundary layer grows and whether or not it separates from the body surface. Both of these factors have significant effects on the aerodynamic forces. Although the transition process in attached shear layers has received a great deal of attention,[19-26] there is, at the present time, no theory of transition to turbulence.[26] On the positive side of this complex problem there are some excellent experiments which show the important physical features of transition.

It is generally agreed that transition from laminar to turbulent flow may be described as a series of events which take place more or less continuously,[27] depending on the flow problem studied. Since turbulence is a three-dimensional phenomenon the breakdown of a two-dimensional laminar flow may be viewed as the process whereby finite amplitude velocity fluctuations, or traveling wave disturbances, acquire significant three-dimensionality.[25] The velocity fluctuation or traveling wave front which is initially straight (for the flow over a flat plate) develops spanwise undulations that are enhanced by second order effects, as depicted in Figure 1. For the flow over a non-spinning axisymmetric body, the traveling wave front is axisymmetric, as indicated in Figure 2. Transition on a flat plate has been very graphically described as the process by which the straight and parallel vortex lines of a two-dimensional laminar flow deform into a constantly changing and twisting three-dimensional mess call "turbulence." This is best described by a quote from Reference 21:

> "It is not the mere presence of vorticity that characterizes turbulence. It is the complexity of the vorticity field. In a laminar boundary layer, the vortex lines are parallel and stacked

2

near the wall, like uncooked spaghetti. In the turbulent layer,
the vortex lines are constantly changing and twisting. Near the
wall, major entanglements appear, and the vortex lines may develop
knots and crossover points. The spaghetti is cooked."

Still photographs and high speed movies of smoke injected into the boundary
layer clearly delineate the details of the complex transition process.

For a spinning axisymmetric body, vortices which originate in the cross-
flow spiral around the body, as shown in Figure 3. These cross-flow vortices
eventually break down into turbulence but do so in a somewhat different
manner from the axisymmetric waves. Depending on the length Reynolds number
and spin rate, the axisymmetric waves initiate the transition process or the
vortices generated in the cross-flow initiate the transition to turbulence.
Furthermore, for certain combinations of these parameters, both the axisym-
metric waves and the cross-flow vortices occur.[28] The simultaneous
occurrence of these two phenomena was first discovered at the University of
Notre Dame, using smoke visualization. Because of the complex nature of
the transition process and the sensitivity of the individual events in this
process, experiments are very difficult. The most important recent contri-
butions to understanding the physics of the transition process have come
from flow visualization experiments.[26] The non-intrusive nature of flow
visualization plus its global view have been important factors in its success.
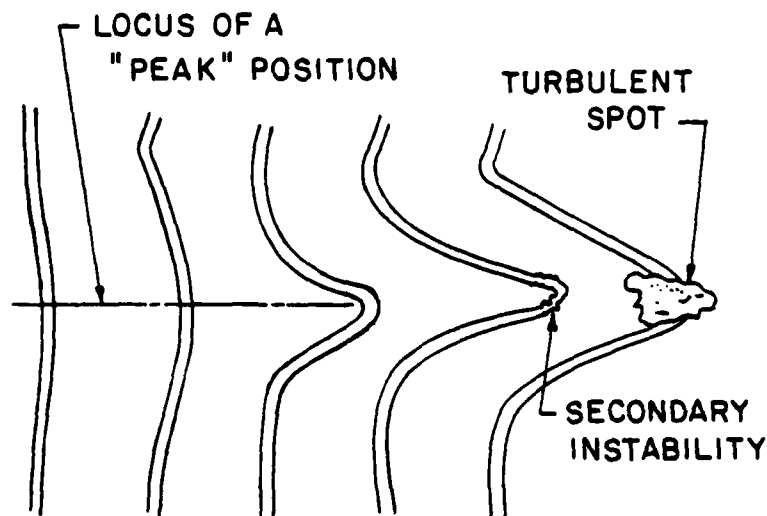
Figure 1. Successive locations of wave fronts in the
later stages of transition (taken from Ref. 25).
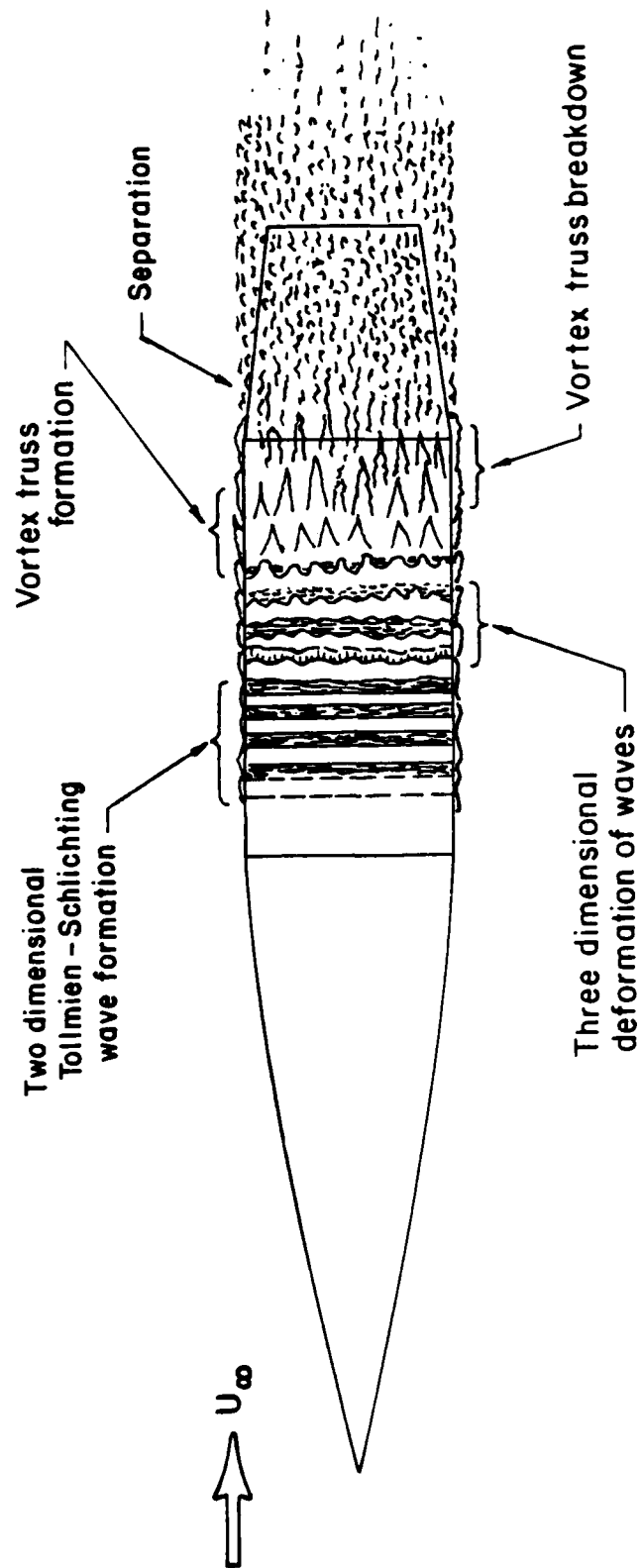
Figure 2. Boundary Layer Transition on a Secant Ogive Nose Axisymmetric Body at Zero Angle of Attack and Zero Spin

4
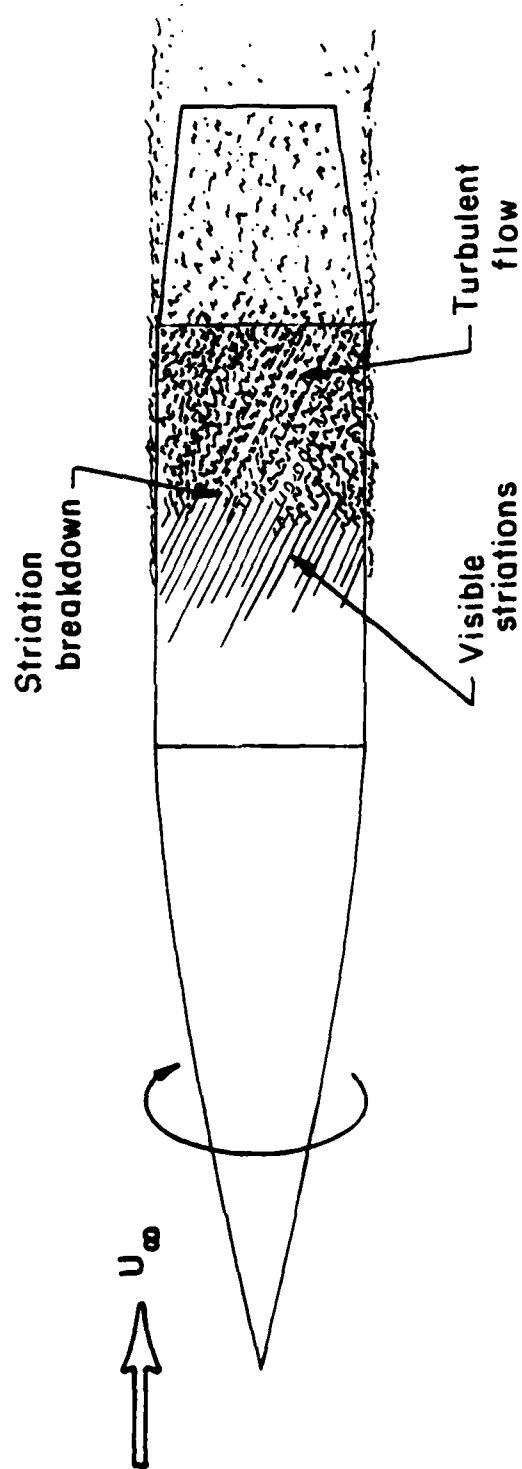
Figure 3. Sketch of the Smoke Striations Resulting from the Cross-Flow
Vortices on the Spinning Axisymmetric Body

5

Scope of Present Work

The primary objective of this research was to obtain a better under-
standing of the effects of spin on the boundary characteristics of secant
ogive nosed axisymmetric bodies. Understanding these characteristics is
important in explaining the Magnus force. To meet this objective, extensive
flow visualization and side force measurement experiments were performed on
axisymmetric models with sharp and 10%, 20% and 30% bluntness ratio secant
ogive noses. The Reynolds number based upon total model length was varied
from approximately 300,000 to 1,000,000, the peripheral to free stream velocity
ratio varied from 0 to 4, and the angle of attack varied from $1°$ to $10°$. A
correlation of the visual and side force data was made.

EXPERIMENTAL APPARATUS

All experiments were conducted in the University of Notre Dame's low
turbulence, subsonic smoke wind tunnels. The indraft tunnel has twelve
anti-turbulence screens which break up small laboratory disturbances,
allowing consistent flow visualization conditions. Larger eddies are broken
up by a 203 mm wide sheet of 19 mm cell diameter hexagonal honeycomb hung
immediately in front of the screens. The 24:1 area contraction inlet is
followed by a 1828 mm long test section with a 610 x 610 mm square cross-
section. The specially designed test section features a plate glass front as
well as glass regions on the top, bottom and back to enable the photographing
of asymmetrical flow conditions. A black velvet-covered back eliminates
reflection of the high intensity lighting conditions. In this tunnel config-
uration, test section velocities can be varied from 5 to 27 m/sec through
the use of the variable speed fan at the end of the diffuser. Figure 4 is
a sketch of the Notre Dame subsonic smoke tunnel.

Smoke for flow visualization purposes was generated by dripping
deodorized kerosene on to electrically heated plates. The smoke was forced
out of the generator by a blower into a smoke rake which filtered out smoke
tars. The smoke temperature was lowered to ambient conditions by use of a
heat exchanger. The smoke exited the rake via a "trombone bell" reduction
cone, and produced a smoke tube which impinged on the model tip and was
entrained in the boundary layer. Reference 29 contains a more complete
description and development of the smoke tunnel facility.

6
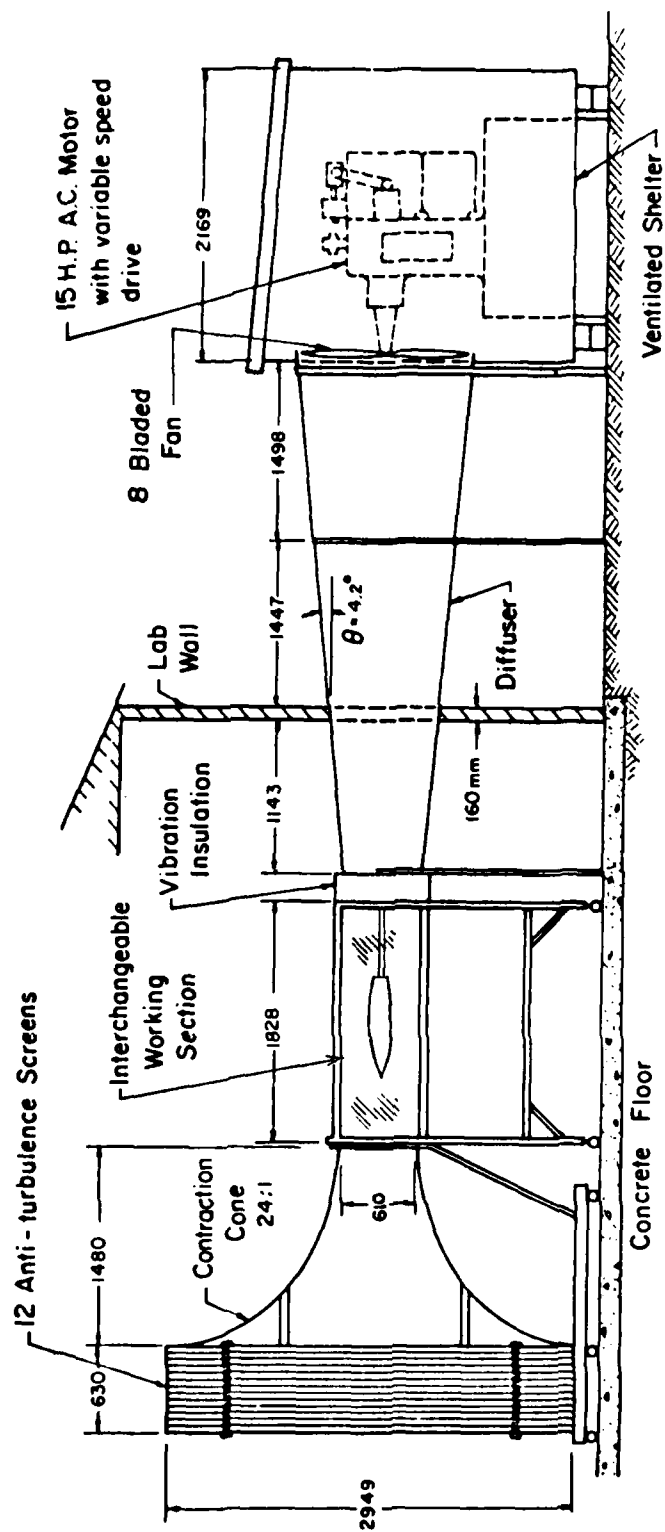
Figure 4. Low Turbulence Subsonic Smoke Tunnel with Axisymmetric Body.

(All Dimensions in Millimeters)

7

Both still and high speed motion picture photography were used to record the flow visualization data. Still photography of the smoke flow was obtained using a Graphlex 101 x 127 mm (4 x 5 in.) camera, synchronized with four high intensity General Radio Type 1532 strobolumes with 20 microsecond duration. Kodak Royal-X film was used. High speed movies were obtained using a Wollensak WF-3 Fastax camera. The Fastex camera, with a speed range from 1,500 to 7,000 frames/sec, was used with several 1,000 and 2,000 watt quartz lights. A Red Lake Laboratories timing light generator was used in conjunction with the Fastex camera to mark the film for more accurate determination of the film speed. Kodak 4-X negative 16 mm movie film was used in the experiments requiring the Fastex camera.

The baseline model for the flow visualization, pressure, and force tests was an axisymmetric model consisting of a 3-caliber secant ogive nose, a 2-caliber cylindrical mid-section, and a 1-caliber 7° conical boattail. Two baseline models were constructed, one to be used for the flow visualization and force tests and the other for measuring the pressure distribution on the body. Each model was constructed from three separate parts. The cylindrical mid-section had internal threads at each end so that the nose and boattail sections could be easily threaded into position. A set of blunted 3-caliber secant ogive nosed sections were also constructed. These nose sections had bluntness ratios (nose to mid-section radii) of 10%, 20% and 30%.

Both baseline models were polished to a surface finish of 0.254 micrometers (10 microinches). For photographic contrast and to minimize reflections, the flow visualization models were anodized black. Figures 5 and 6 are drawings of the baseline model and the blunt-nosed shapes used in this investigation.

To spin the model for both visualization and side force studies, a sting arrangement was designed to simplify data gathering. Initially, a high pressure nitrogen gas was pumped through the sting to an air turbine mounted inside the model to induce spin. To conduct tests, the model would be run over the desired rpm with the data being gathered while coasting through the desired spin rate. The present design, Figure 7, enables much better control of the spin rate through the use of a feedback control circuit. A timing disk enables the desired spin rate to be easily set with the reostat.

8
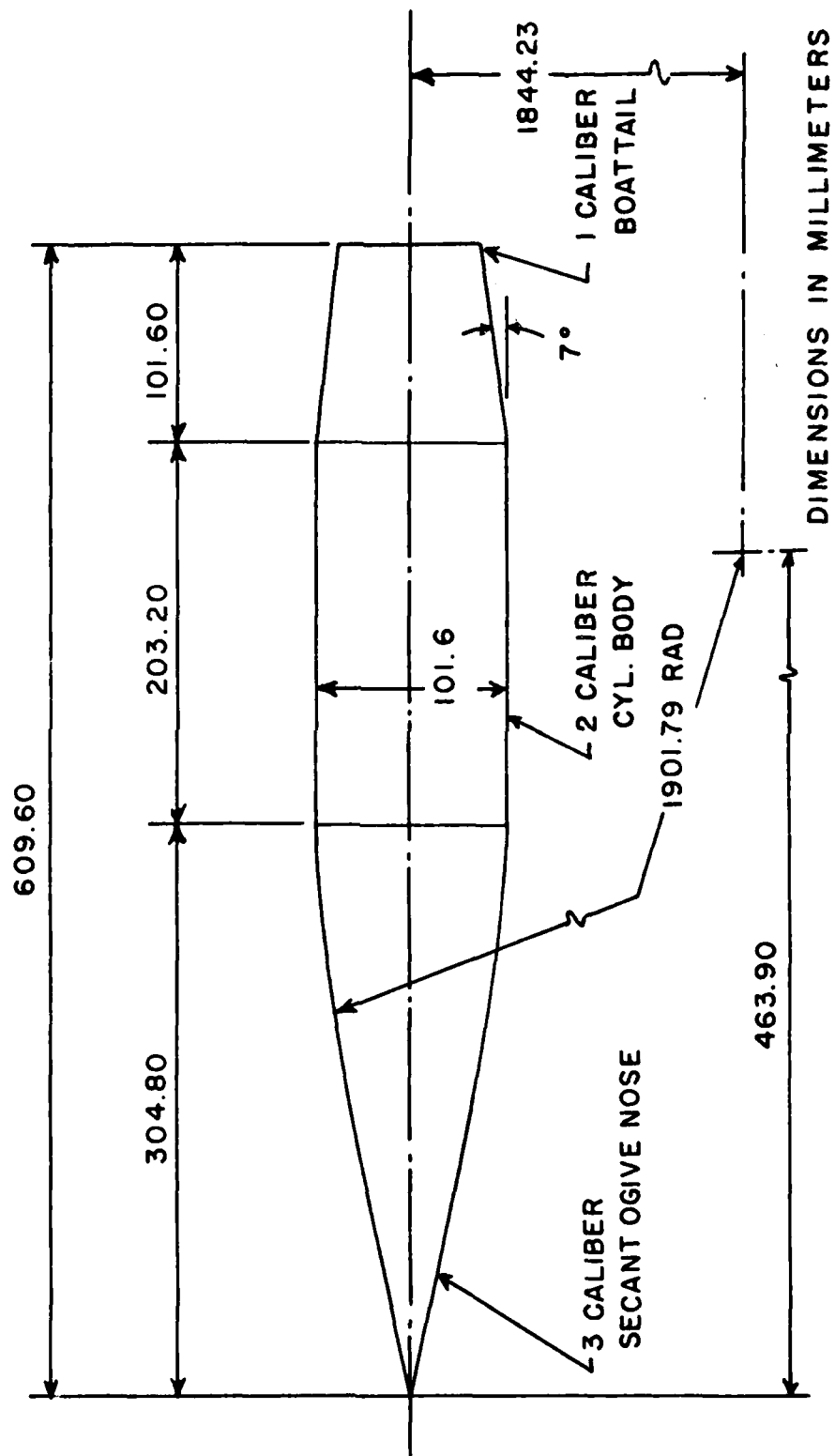
Figure 5. Baseline Wind Tunnel Model

10% BLUNTNESS RATIO

20.63   284.17

Radius = 5.08

20% BLUNTNESS RATIO

43.35   261.45

Radius = 10.16

30% BLUNTNESS RATIO

66.30   238.50

Radius = 15.24
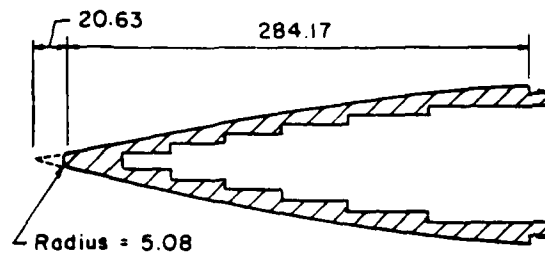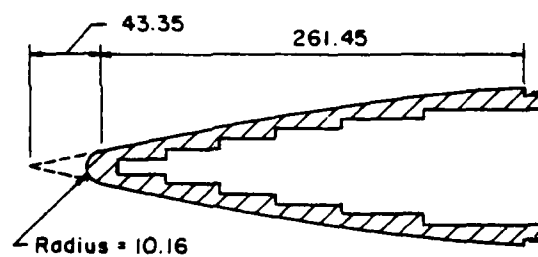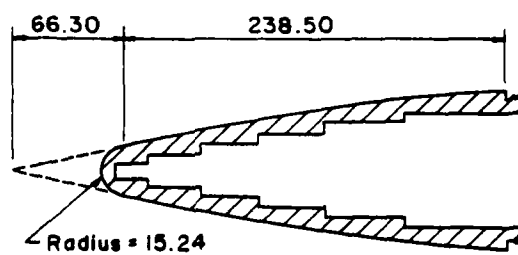
Dimensions in millimeters

Figure 6.   10%, 20% and 30% Bluntness Ratio Nose Sections

10
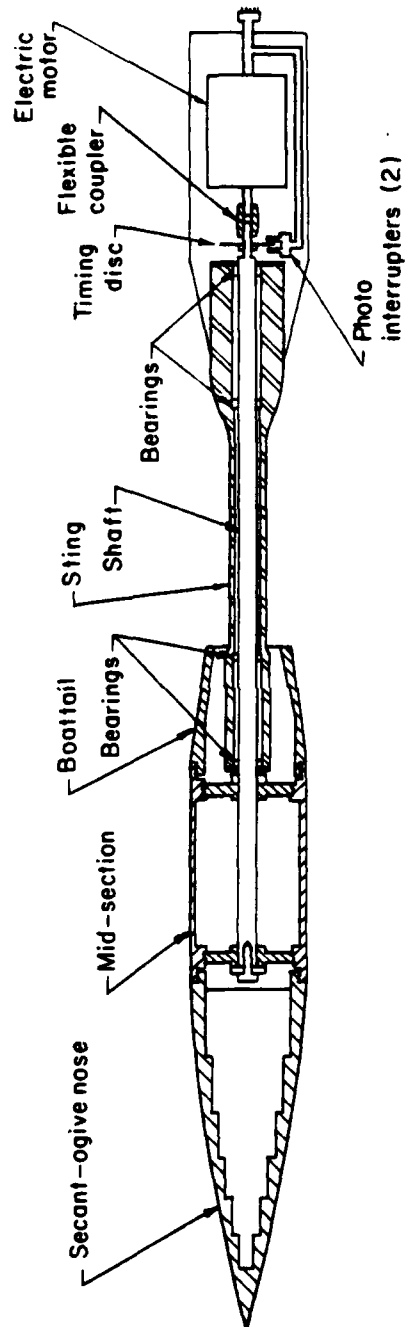
Figure 7. The Baseline Secant Ogive Nose Flow Visualization and Side Force Model and Drive System

11

Four SBB model TCNR 12-16-3 ultra-precision radial ball bearings, two mounted within the sting in the model boattail and two mounted near the rear of the sting near the timing disk, allow for smooth, vibration-free spin operation of the model up to 9,000 rpm.

Side force measurements were made using a strain gauge force balance mounted atop the test section. The strain gauge in the balance and bridge amplifier circuit yielded an analog voltage output corresponding to the side force. The balance was calibrated in a range of 0 to 5 Newtons and was accurate to within ±0.01 Newton, making very sensitive measurements possible.

The Scanivalve pressure sampling scanner and the low range pressure transducer were the principal elements used in obtaining the pressure data. This capacitance type of sensor converts changes in capacitance due to pressure variations into a high level, low impedance D.C. output voltage signal. The output voltage corresponds to the difference between the pressure at each tap location along the model and the tunnel static pressure, P_∞. The data were manually recorded and reduced to pressure coefficient form. Figure 8 is a drawing of the pressure model.

RESULTS FROM THE SHARP NOSED MODEL

The ultimate objective of this boundary layer study was to develop a "physical" picture of the flow field associated with spinning and non-spinning axisymmetric bodies. It is hoped that this physical picture of the boundary layer will lead to improved flow field models.

The research was conducted in several phases. The first phase was the investigation of the boundary layer development on the non-spinning baseline model at zero angle of attack. During the second phase, the effect of spin on the boundary layer was documented at both angle of attack and zero angle of attack. Finally, the influence of nose bluntness was investigated for all the above cases.

Non-Spinning Model at Zero Angle of Attack

Flow visualization and pressure data were obtained on the baseline model for Reynolds numbers (based upon model length) from 315,000 to 1,030,000. Although this was a rather narrow range of Reynolds numbers, the phenomena occurring on the model varied dramatically. At the lowest

12
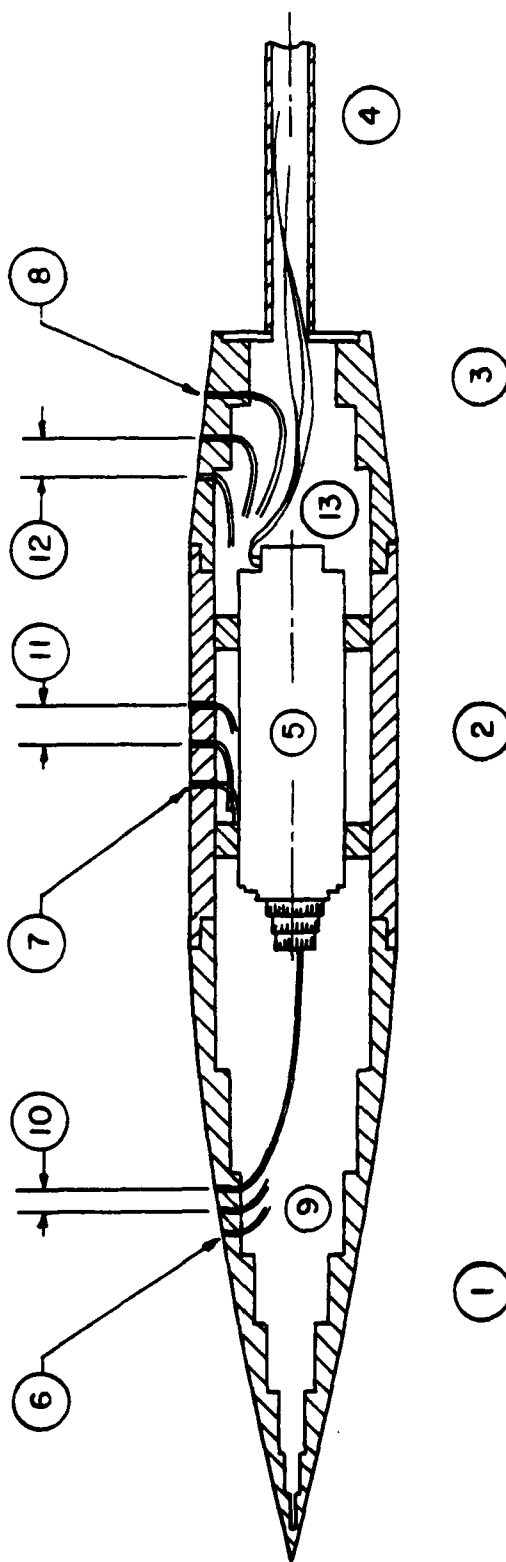
1. SECANT OGIVE NOSE
2. CYLINDRICAL BODY
3. BOATTAIL
4. STING
5. SCANIVALVE

6. 30 PRESSURE TAPS 1.27 m.m. I.D.
7. 12 PRESSURE TAPS
8. 6 PRESSURE TAPS
9. 1.27 m.m. I.D. TYGON TUBING
10. 10.16 m.m.

11. 20.32 m.m.
12. 20.32 m.m.
13. SCANIVALVE WIRES

Figure 8. The Baseline Secant Ogive Pressure Model

13

Reynolds number, 315,000, the flow remained laminar over the entire body, with separation occurring at 0.75-caliber down the boattail, as shown in Figure 9a. As the flow separated, axisymmetric vortex rings were shed periodically into the wake. The rings were shed at a frequency of approximately 120 rings/sec. There also appeared to be a very slow recirculative region near the surface of the boattail.

For the Reynolds number 631,000, two-dimensional Tollmien-Schlichting waves were observed intermittently along the cylindrical body. These waves disappeared as they approached the body-boattail intersection. It was observed that the separation point had moved up the boattail to about 0.5-caliber, as shown in Figure 9b. The axisymmetric vortex rings were shed as before; however, they accelerated more rapidly into the free stream just after separation. As shown in Figure 10, there is a marked difference in the pressure profiles along the boattail for the two lower Reynolds number flows.

At a Reynolds number of 814,000, two-dimensional Tollmien-Schlichting waves formed continuously at the mid-point along the body and disappeared just before the boattail. Separation occurred at a position 0.3-caliber along the boattail and axisymmetric vortex rings appeared in the wake, as illustrated in Figure 11a. The shedding pattern was quite similar to that for the Reynolds number 631,000 flow; however, the rings broke down earlier into a turbulent wake. At a Reynolds number of 928,000, two-dimensional Tollmien-Schlichting waves formed continuously. Approximately 50% of these waves broke down to form vortex truss patterns. The flow along the boattail became turbulent following the intermittent formation of the trusses. When trusses did not appear, axisymmetric vortex rings were shed and rapidly broke down, as shown in Figure 11b.

At the highest Reynolds number studied, $R_L = 1,030,000$, the transition process was found to be similar to the results obtained by F.N.M. Brown and his colleagues on a tangent ogive nosed body.[27] The development of the transition process on a _tangent_ ogive nosed axisymmetric body is illustrated in Figure 12a. For the highest Reynolds number, all phases of the transition process were present. Figure 12b is a photograph of the boundary layer at the highest Reynolds number. This transition phenomenon was observed and

14
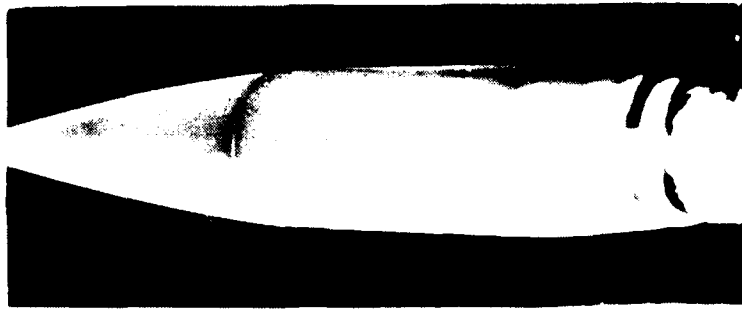
Figure 9a. Smoke Photograph for R_L = 315,000,
0 rpm, α = 0°.
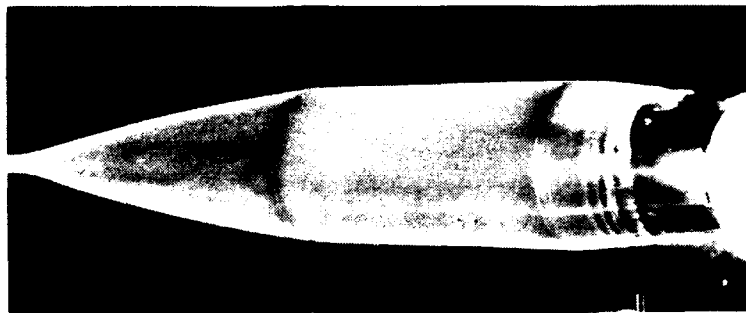
Figure 9b. Smoke Photograph for R_L = 631,000,
0 rpm, α = 0°.

ZERO ANGLE OF ATTACK
NON − SPINNING

—— R_L = 631,000

— — R_L = 315,000

Note: The C_p scale used in reference 12 is incorrect.
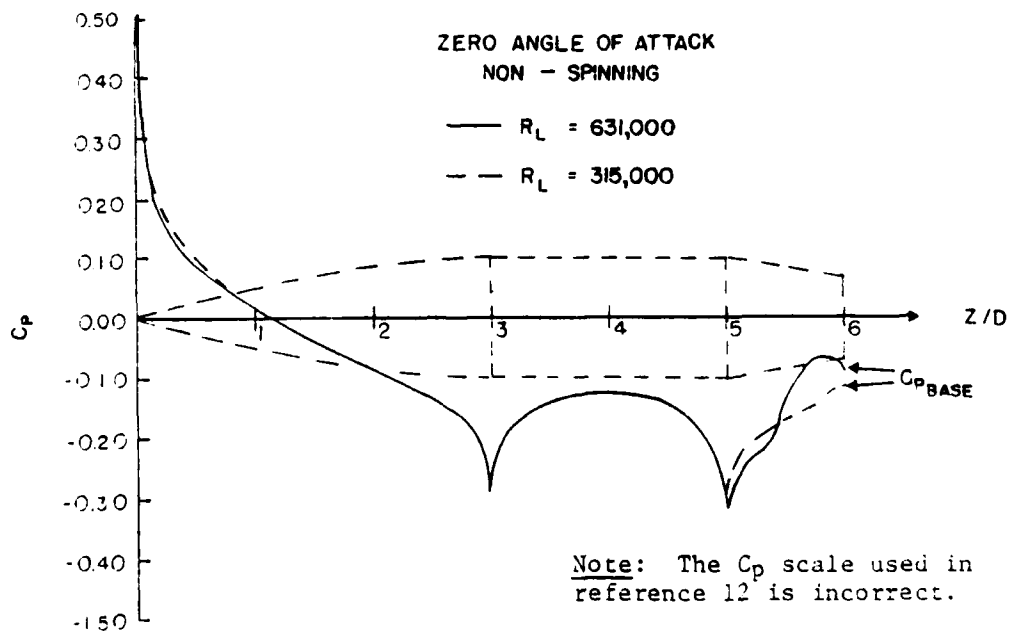
Figure 10. Pressure Distribution along the Baseline
Model at Zero Angle of Attack (R_L = 315,000 and 631,000)
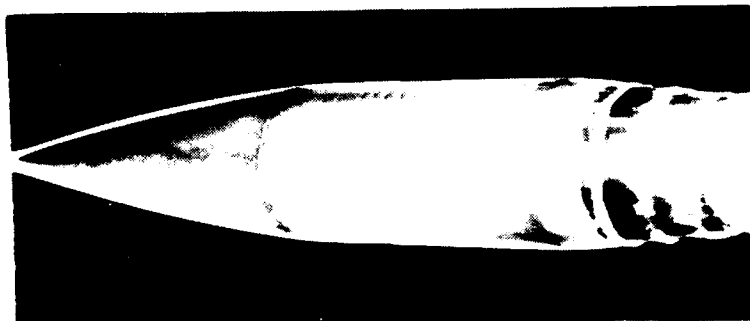
Figure 11a. Smoke Photograph for R_L = 814,000,
0 rpm, α = 0°.

Figure 11b. Smoke Photograph for R_L = 928,000,
0 rpm, α = 0°.

Formation of a set of two-dimensional waves

Region R₁

Three-dimensional deformation of waves

Region R₂

Region of vortex trusses

Region R₃
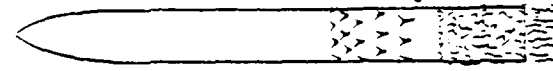
Breakdown of vortex trusses into
region of turbulence

Region R₄
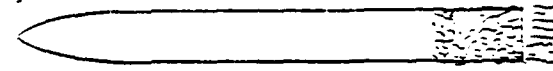
Laminar region following breakdown

Region R₁₋₄
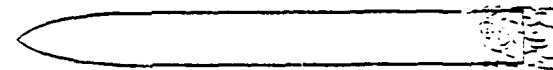
Reappearance of two-
dimensional waves   Region R₁

Figure 12a.   Time Development of Boundary Layer
              Transition (one cycle) (Ref. 27)
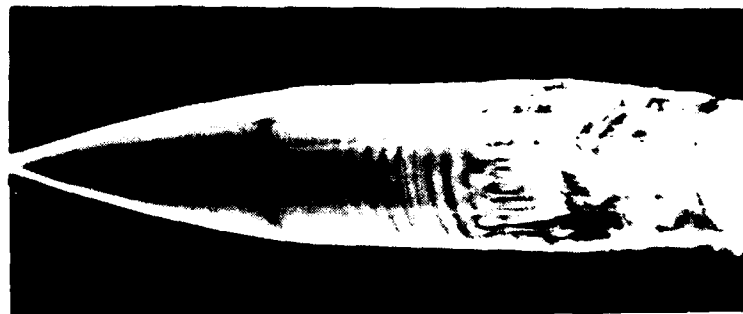
Figure 12b.   Smoke Photograph for R_L = 1,030,000.
              0 rpm, α = 0°.

recorded using high speed smoke photography. The camera was set at 3,000 frames/sec and the timing light at 1,000 cycles/sec. The timing marks were used to determine when the camera achieved the desired speed. The two-dimensional waves, region R_1 of Brown (Figure 12a), were first observed at the mid-section of the cylindrical portion of the model. It appeared that three to five strong (i.e., larger amplitude) waves were formed, followed by two to three weaker ones. Depending on the strength of the two-dimensional waves, trusses (region R_3 of Brown) were formed anywhere from 0.9 to 1.75-caliber along the mid-section of the body. Region R_2 of Brown, the three-dimensional deformation of the waves, was not always visible since the flow passed through this region to the truss formation stage so quickly. The wave spacing was found to be approximately 0.13-caliber per wave. However, this wave length was found to range from 0.11 to 0.15-caliber. The wave speed was estimated to be about 10 m/sec for the free stream velocity of 25.5 m/sec. It was observed that almost all the two-dimensional waves became three-dimensionally unstable and formed truss patterns before leaving the cylindrical portion of the model. However, approximately 5% did not form trusses and were simply washed downstream.

Groups of two to five two-dimensional waves, almost simultaneously, became unstable and formed trusses. Because the breakdown of the two-dimensional waves occurred so rapidly, the three-dimensional wave pattern observed by Brown was only apparent in some of the photographs. Most of the trusses which developed were arranged in a staggered formation, as shown in Figure 13. The truss formation was immediately followed by a breakdown in the truss structure and the diffusion of the smoke into the developing turbulent boundary layer. This is shown in Figure 14.

The pressure distributions for all five Reynolds numbers were very similar, with the only significant differences occurring along the boattail. The pressure distributions shown in Figures 10 and 15 are typical for this model configuration. The C_p is equal to 1 at the tip of the nose and decreases continuously along the nose. A sharp spike in the pressure distribution occurs at the nose-body intersection. The pressure then increases along the center body, reaching a maximum at the mid-point. This adverse pressure gradient is favorable to the amplification of disturbances

18
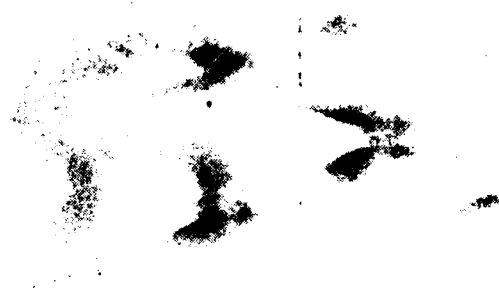
Figure 13.   Enlargement of Vortex Truss Pattern
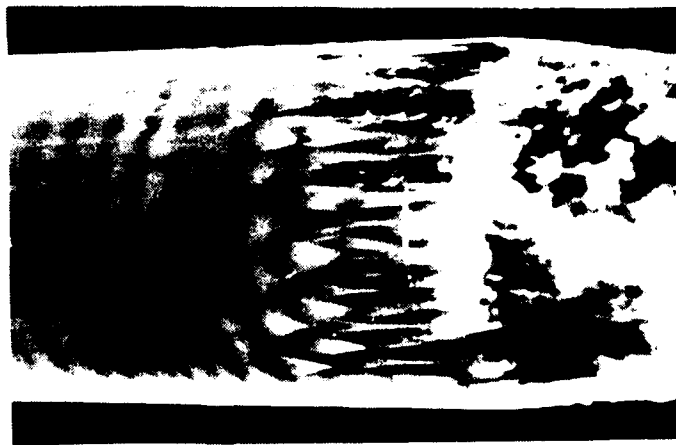
Figure 14.   Enlargement of Transition Region
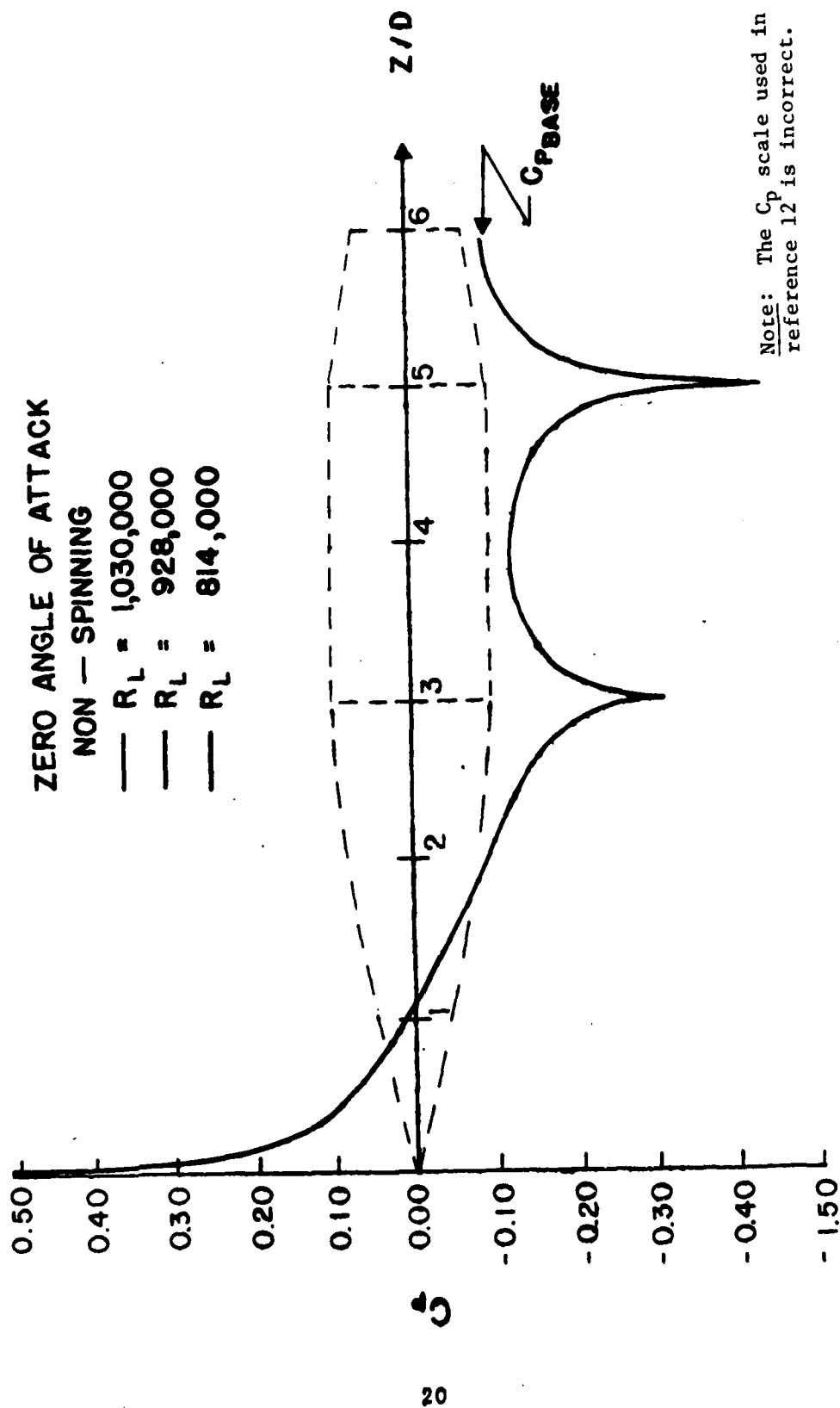
Figure 15. Pressure Distribution along the Baseline Model at Zero Angle of Attack (R_L = 814,000, 928,000 and 1,030,000)

in the boundary layer. This is the region where the two-dimensional waves were observed in the smoke pictures for all but the lowest Reynolds number flow. The pressure distribution has a second and larger spike at the juncture between the body and the boattail. This spike would indicate that the flow is accelerating across the region, demonstrated in the smoke pictures by the stretching of the vortex truss patterns. The pressure along the boat-tail increases rapidly up to the separation point. As mentioned, there are significant differences in both the pressure data and the observed phenomena along the boattail at the Reynolds numbers 315,000 and 631,000. The three highest Reynolds numbers produce approximately the same pressure profiles and separation point locations, as shown in Figure 15.

Spinning Model at Zero Angle of Attack

Still photographs were taken of the baseline model at an angle of attack of zero over a Reynolds number range from 315,000 through 1,030,000, and spin rates from zero through 4,500 rpm. The transition process over the spinning model took a vastly different form from that of the non-spinning case. Transition on the non-spinning model originates as a viscosity-controlled two-dimensional Tollmien-Schlichting type of instability. The transition process on the spinning model bears resemblance to instabilities which occur on both the rotating disk[30] and the swept wing.[31] A typical example of this spin-induced transition process is shown in Figure 16. The phenomenon was primarily related to the ratio of the peripheral velocity to the free stream velocity, V/U_∞, and relatively independent of Reynolds numbers (i.e., it was not significantly affected by changes in Reynolds number for a given V/U_∞). Experiments were conducted for a range of V/U_∞ between zero and 3.9. There were no visible changes in the boundary layer characteristics for V/U_∞ less than 0.4, with the exception of a slight skewness in the tips of the vortex trusses. When vortex trusses were present, this skewness could be seen for V/U_∞ values as low as 0.1, as shown in Figure 17. As V/U_∞ increased, striations in the smoke[32] appeared at an angle approximately equal to $\tan^{-1}$ of V/U_∞, as shown in Figure 18. The striations are a manifestation of vortices originating in the cross-flow. The wave length of these striations, λ/D, was approximately 3.8×10^{-2} and remained constant regardless of V/U_∞, spin rate or Reynolds number for the cases studied. As the Reynolds number was increased, the transition process

21
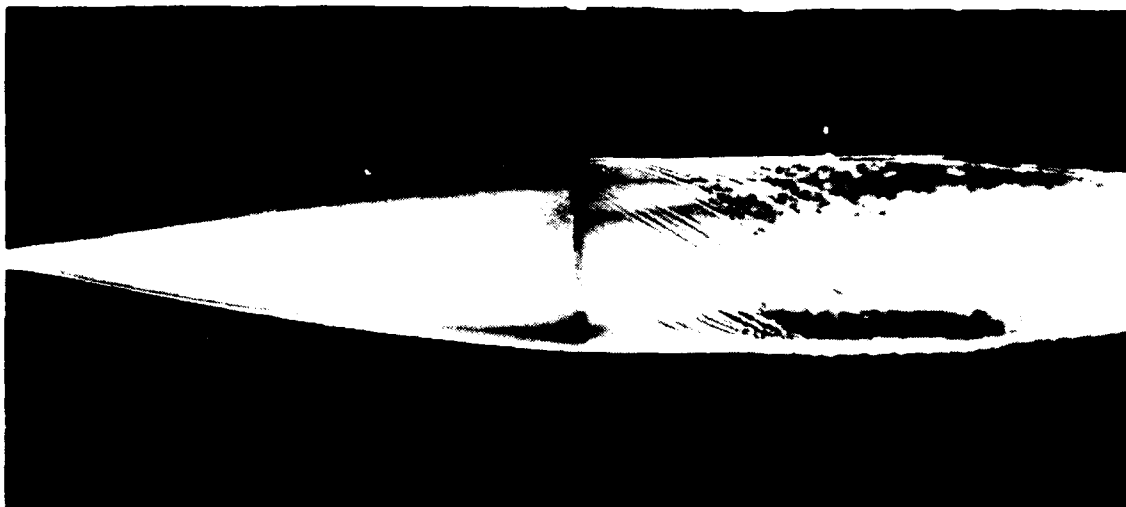
Figure 16.   Spin-Induced Transition at Zero Angle
of Attack (V/U_∞ = 0.658, R_L = 928,000)
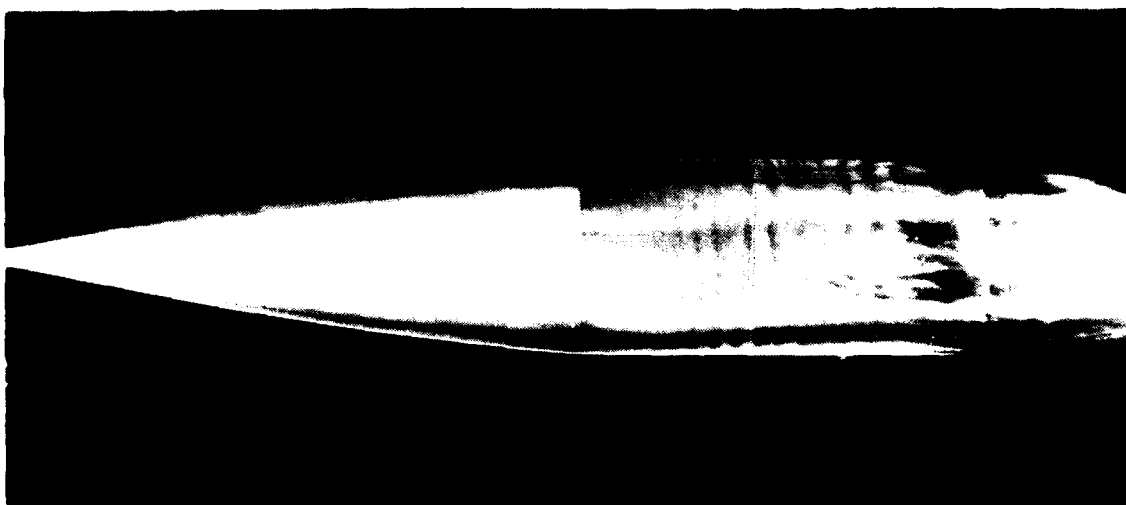
Figure 17.   Smoke Photograph of Spinning Model at Zero
Angle of Attack (V/U_∞ = 0.119, R_L = 1,030,000)
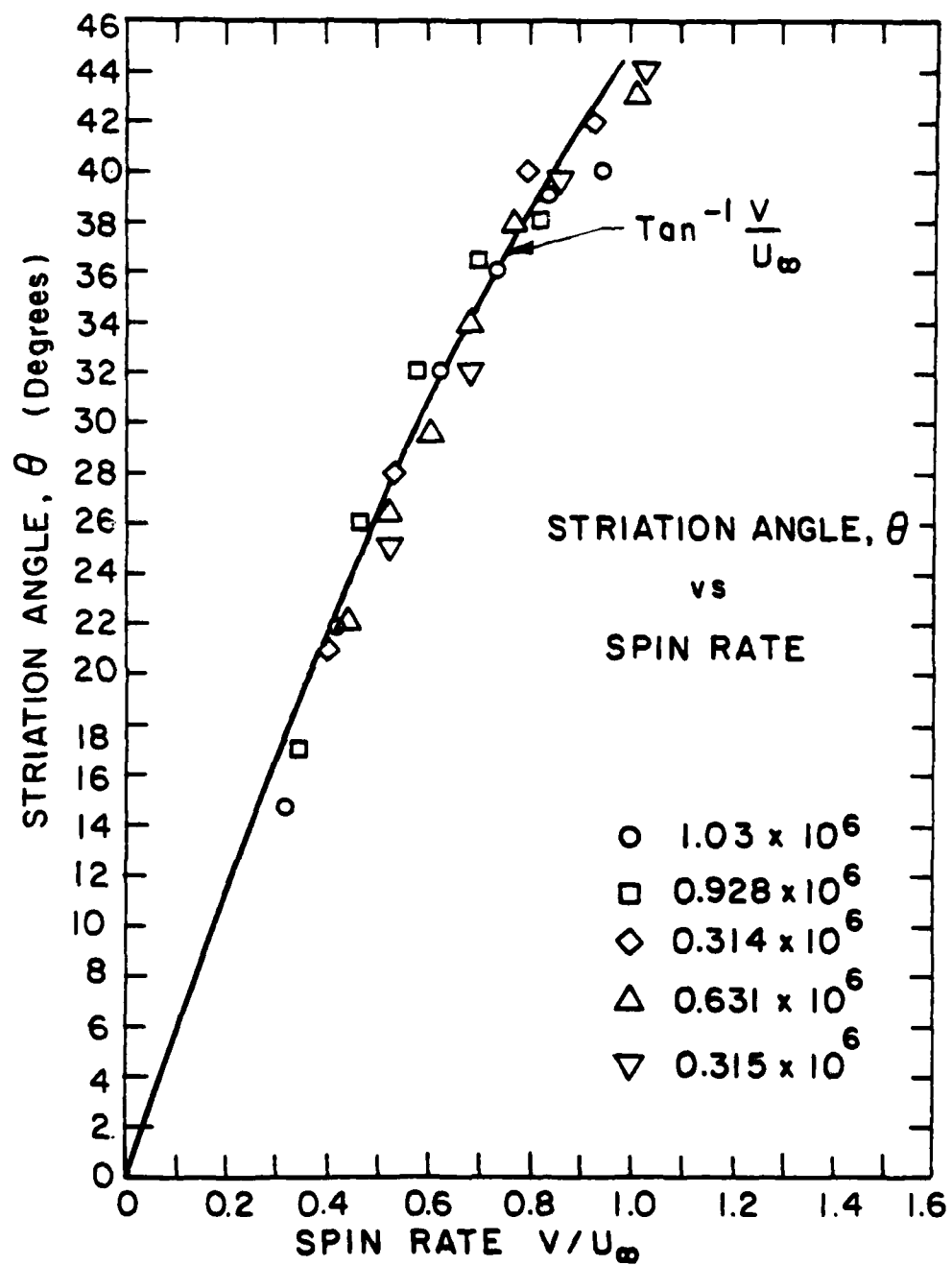
Figure 18. Plot of Measured Striation Angle
versus Spin Rate

took place over a shorter distance. The striations broke down into beads or knots just before becoming turbulent, as shown in Figure 19.

The direction of rotation of the model is not obvious from the appearance of the striations. If one were to leave a trail on the model with a paint brush, moving the brush only in the direction of the free stream (from nose to tail) while the model was spinning clockwise (facing upstream), one would leave a trail along the model at the striation angle, $\tan^{-1} V/U_\infty$. The striations, however, are not on the surface of the model. It appears that these striations are manifestations of vortex lines, presumably with a sense of rotation opposite from that of the model. They are formed at a distance from the model where the cross-flow becomes unstable. Bear in mind that the phenomena in the smoke photographs represent a Lagrangian point of view, or streakline portrayal of the flow field.

The location of the transition zone is largely a function of V/U_∞. For a constant rpm, the transition zone moved forward with decreasing Reynolds number. The transition zone moved forward with increasing spin rate as anticipated at a constant Reynolds number. Furthermore, when the striations appeared towards the end of the mid-section they were superimposed on the two-dimensional, axisymmetric Tollmien-Schlichting waves. The simultaneous occurrence of the Tollmien-Schlichting waves and the vortices spiralling around the body, to the authors' knowledge, were first observed in Notre Dame's smoke tunnel. These phenomena are the subject of further study. At high values of V/U_∞ (V/U_∞ greater than 1.0), the boundary layer was fully turbulent along the entire mid-section, regardless of Reynolds number. Figure 20 shows spin-induced turbulence occurring at the lowest Reynolds number tested ($R_L = 315,000$) at a velocity ratio of 1.55.

Spinning Model at Angle of Attack - Side Force Measurements

Magnus force data were obtained for the baseline model for Reynolds numbers of 315,000 and 1,030,000 based upon the body length. The angle of attack of the model was varied from 0° to 10° in two degree increments, and the non-dimensional velocity ratio, V/U_∞, was varied from 0 to 3.9. The data exhibited both positive and negative side forces over the spin rates studied. The side force measurements were reduced and plotted in non-dimensional form. The coordinate system used in the analysis of the data

24

Figure 19. Enlargement of Striations Illustrating
Striation Breakdown
$(V/U_\infty = 0.825, R_L = 814,000)$
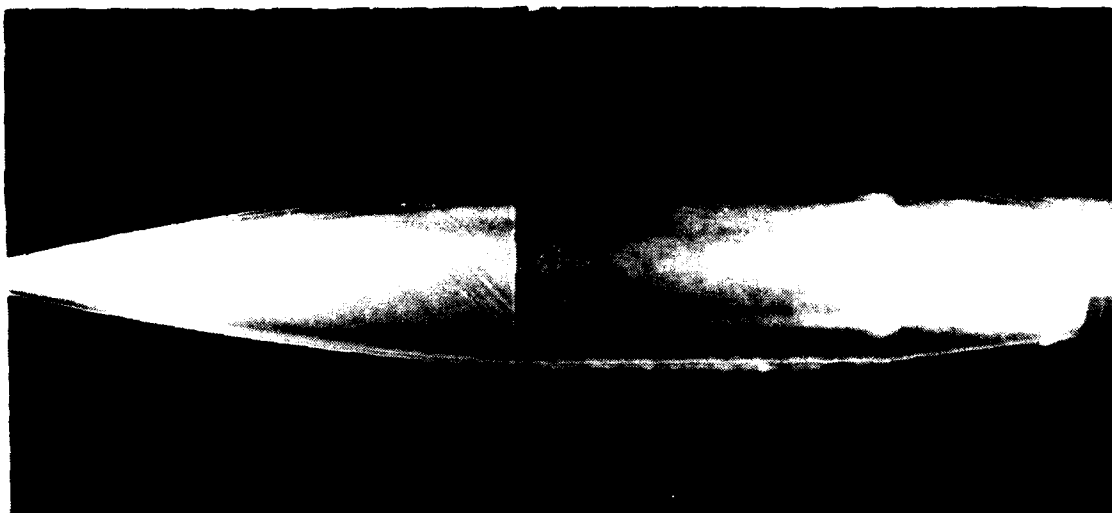
Figure 20. Smoke Photograph of Spinning Model at
Zero Angle of Attack, Illustrating Spin-Induced
Turbulence at Lowest Reynolds Number Studied
$(V/U_{\infty} = 1.55, R_L = 315,000)$

is shown in Figure 21. The non-dimensional side force coefficient, C_y, was plotted versus velocity ratio, V/U_∞.

It is necessary to understand the orientation of the x, y and z axes before proceeding further. The x axis coincides with the axis of rotation of the model and is positive, facing upstream. The z axis is in the plane of the velocity vector and the x axis (the vertical plane), and is perpendicular to the x axis, positive downward. The y axis is then bi-normal to the x and z axes, positive to the right or starboard side of the model, and forms a right-hand set. Note that for a positive angle of attack, the cross-flow component of the velocity vector is in the negative z direction. Thus, for a positive rotation (clockwise, facing upstream), the classical Magnus force acts in the negative y direction. Conversely, a positive side force coefficient, C_y, acts in the negative Magnus force direction.

For both Reynolds number cases, a zero angle of attack/zero side force verification test was conducted using the sharp nosed baseline model. Figure 22 displays relatively flat curves of C_y versus V/U_∞ or a negligible side force generated throughout the spin rate range, as expected. Any small waverings about the x axis were caused by a slight but random electronic drift in the strain gauge amplifier circuit.

The 315,000 Reynolds number side force data, at 2° angle of attack, very closely resembled the zero angle of attack verification (i.e., C_y approximately equal to zero). This reinforced an observation made during preliminary tests when the model was misaligned approximately 0.5° to both starboard and port at a particular angle of attack, with little measurable affect on the spin-induced side force. At higher angles of attack, however, starting with 4°, a small bump in the side force curve to the negative Magnus side or positive side force values was observed at low spin rates.[33,34] It originated at a spin rate of about 200 rpm or at a velocity ratio of 0.2, and extended to 700 rpm or a V/U_∞ of 0.5 for the 4° case. At higher spin rates, a relatively linear curve of constant negative slope extends below the x axis or into the negative side force region. Figure 23 displays this trend for the sharp nosed model at angles of attack of 4°, 6°, 8° and 10° where the basic form of the side force curve at each angle of attack is similar. As the angle of attack is increased, the positive side force bump grows both in

27
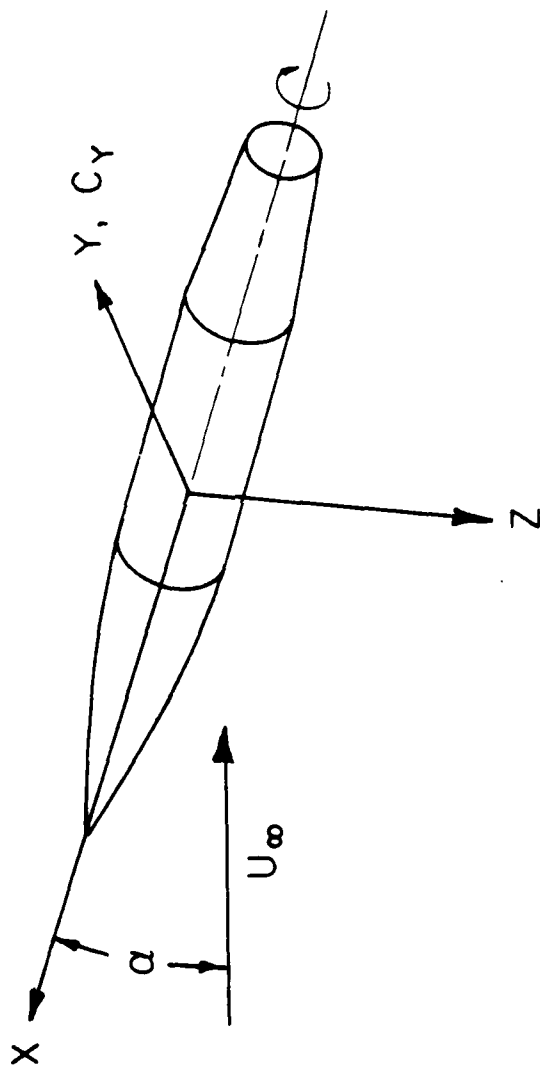
Figure 21. Model Coordinate System
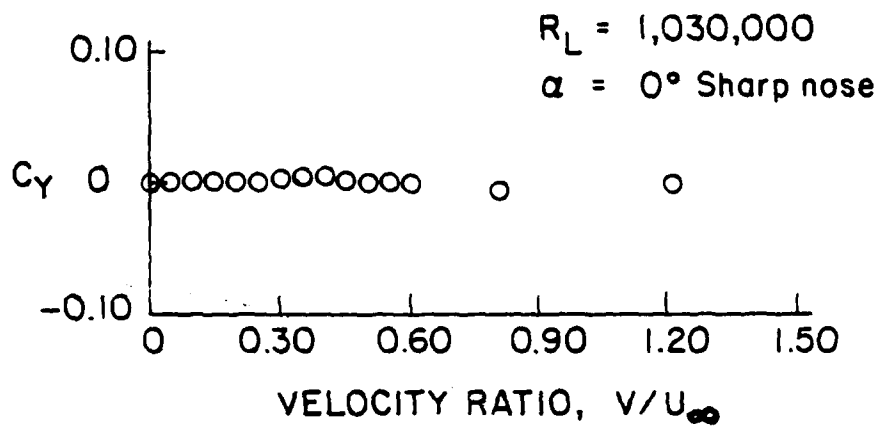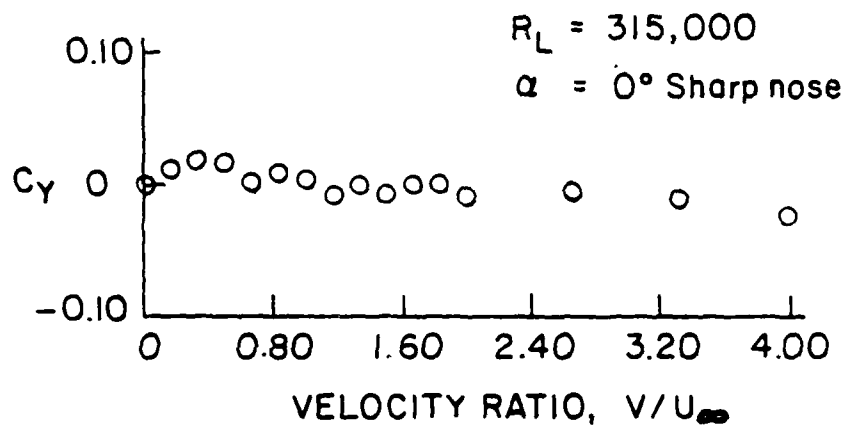
Figure 22.   Side Force versus Velocity Ratio for
Zero Angle of Attack - Sharp Nose

29

$R_L = 315,000$

Sharp nose

○ 4°
○ 6°
□ 8°
◇ 10°

0.20
0.10
0
-0.10
-0.20
-0.30
-0.40

C_Y

0   0.80   1.60   1.40   3.20   4.00
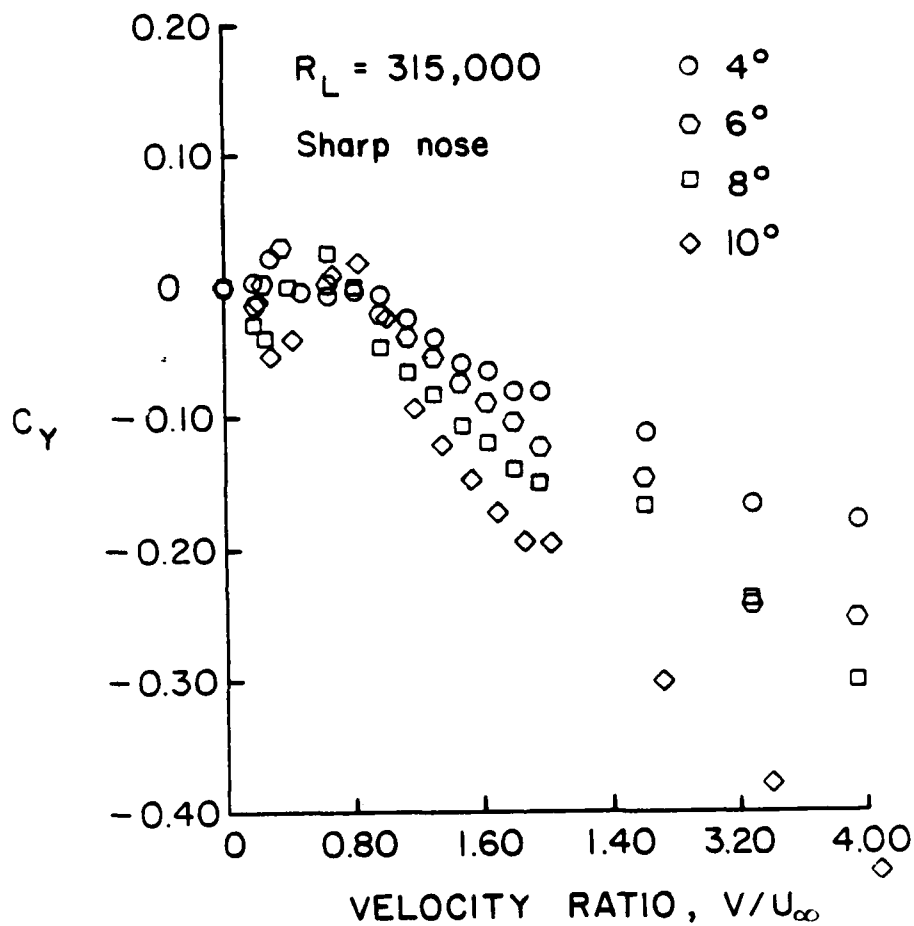
VELOCITY RATIO, V/U_∞

Figure 23.   Side Force versus Velocity Ratio for
$\alpha = 4°$, $6°$, $8°$ and $10°$ – Sharp Nose,
$R_L = 315,000$.

30

amplitude and range of spin rate over which it stretches, and moves to the
right along the x axis. As will be shown in the smoke visualization photo-
graphs, this bump is the result of an asymmetric transition region on the
starboard side of the model. From the above figures, it is suggested that
increasing angle of attack increases the size of the transition region and
delays its movement down the starboard side of the model until a higher spin
rate is achieved. This is due to the increased cross-flow velocity component
which opposes the rotation of the model on the starboard side. Such
observation is verified by a smoke photograph angle of attack sequence as in
Figures 24a, b, c and d at 400 rpm for 4°, 6°, 8° and 10°, respectively.
Additionally, the curves at higher angles of attack have steeper or more
negative slopes in the velocity ratio region just past the asymmetric
transition bump. At high spin rates, larger negative side force coefficients
occur with increasing angle of attack.

The side force characteristics for the high Reynolds number, 1,030,000,
were essentially identical to those of the low Reynolds numbers for a given
nose and angle of attack, as shown in Figure 25. However, the maximum angular
velocity attainable was 6,000 rpm, which corresponded to the maximum velocity
ratio of 1.17 at a Reynolds number of 1,030,000. Little can be said regarding
the effects of velocity ratios greater than 1.17 at R_L = 1,030,000. However,
for spin rates less than 1.17, the side force as a function of velocity ratio
was essentially the same as that for the low Reynolds number. It was evident
that the Magnus force characteristics were relatively independent of Reynolds
number over the range studied for a given velocity ratio.

Smoke Photographs

Smoke photographs provide a visual observation of the boundary layer
development and transition. When correlated with the side force data, the
flow visualization presented a more complete understanding of the transition
phenomenon and the trends in the side force data.

Smoke photographs were taken of the spinning model at various angles of
attack for the lowest Reynolds number (315,000) and highest Reynolds number
(1,030,000). The angles of attack and spin rates chosen were identical to
those at which force data were taken. Starboard (right-hand side), port
(left-hand side) and windward (bottom) views of the model were photographed

31
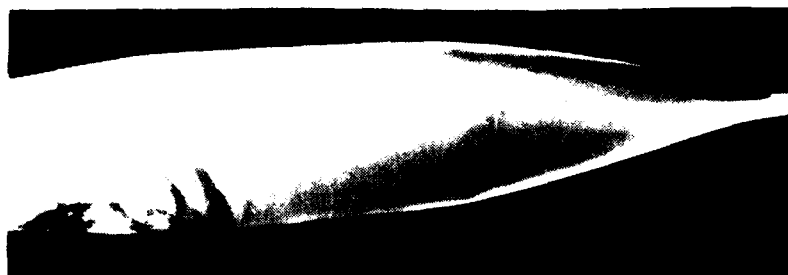
a)　$\alpha = 4°$

b)　$\alpha = 6°$

c)　$\alpha = 8°$

d)　$\alpha = 10°$

Figure 24.　Smoke Visualization of Angle of Attack Effect at a
Camera Axis 55° from Flow Direction Facing Upstream for:
R_L (Sharp Nose) = 315,000, 400 rpm, V/U_∞= 0.304
(Starboard View)
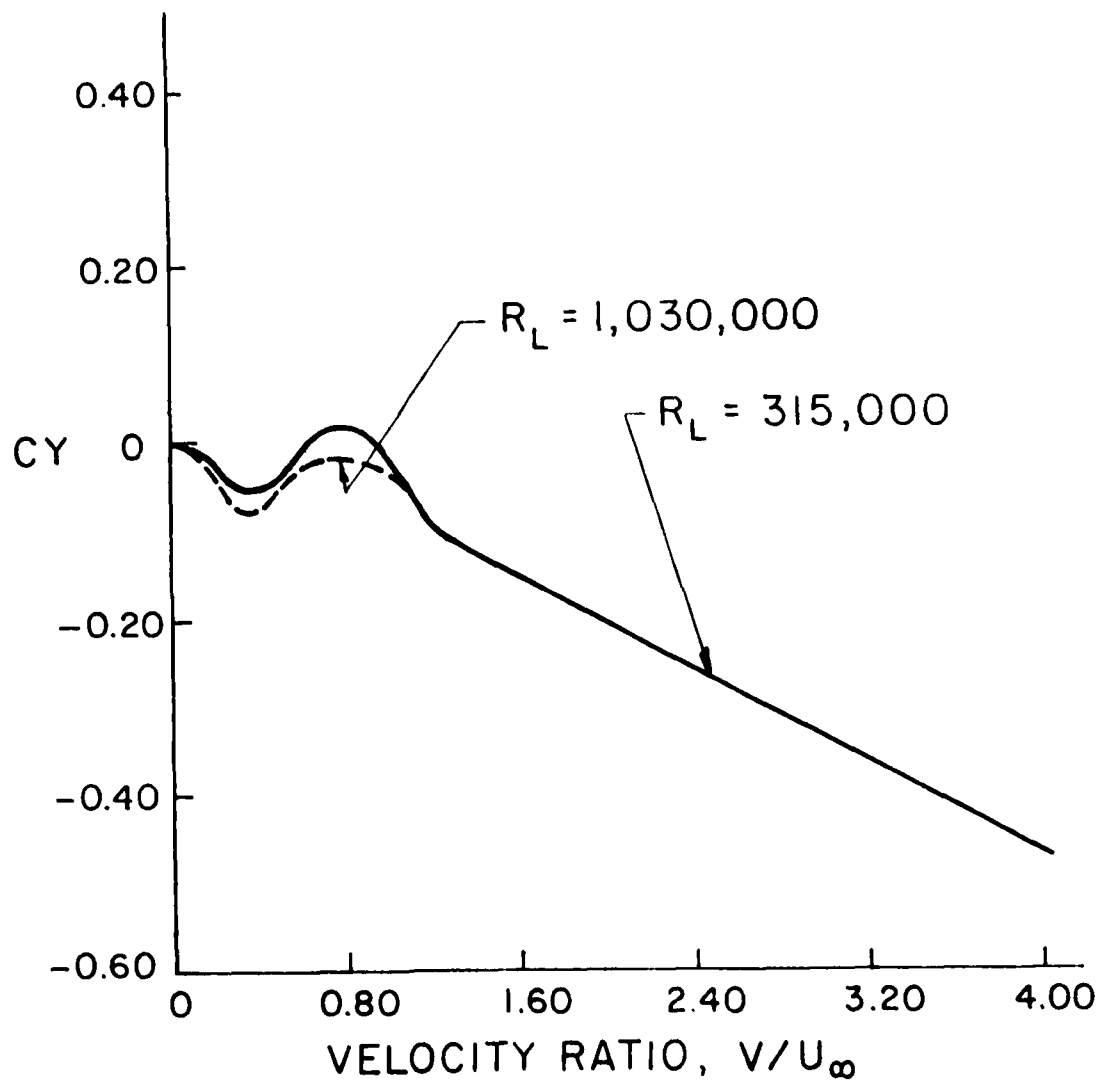
Figure 25.   Side Force versus Velocity Ratio
Reynolds Number Comparison
Sharp Nose, $\alpha = 10°$.

33

to fully document the asymmetries in the boundary layer. Figure 26 shows a series of smoke photographs for various spin rates at an angle of attack of 2° and R_L = 315,000. When the model was not spinning at 2° angle of attack, the boundary layer was symmetrical about the model axis, as shown in Figure 26a. The boundary layer appeared to remain laminar along the entire model, with separation occurring in the form of vortex rings or "doughnuts" being shed from the boattail. The boundary layer closely resembled that of the non-spinning model at zero angle of attack. As spin rate was increased, very long striations in the smoke began to form at an angle equal to $\tan^{-1} V/U_\infty$. Figure 26b illustrates striations, 2-calibers in length, forming on the mid-section for a velocity ratio of 0.678. The boundary layer was symmetrical about the axis of rotation. The smoke photographs agree well with the side force data at 2° angle of attack. As the spin rate was further increased, the striations became shorter and appeared to originate close to the nose of the model. Figure 26c illustrates the symmetrical boundary layer transition for a velocity ratio of 1.02. Figure 26d shows the transition process at the velocity ratio of 1.69. The striations originated symmetrically on the nose and became turbulent within a half caliber. The striation angle was no longer equal to the $\tan^{-1} V/U_\infty$ but was slightly smaller. The radius of the nose where the striations occurred was less than the radius of the mid-section; therefore, the surface velocity of the nose where the striations occurred was less than V, defined as the surface velocity of the mid-section.

A detailed visual study was made of both the port and starboard views of the sharp nosed model at 4° angle of attack. Figure 27 displays the boundary layer for the sharp nose at the low Reynolds number, 315,000, at 4° angle of attack and zero spin rate. It is the smallest angle for which the asymmetric transition region was observed. At the rear of the boattail a small disturbance was visible on both the port and starboard sides of the model (the starboard view is shown in Figure 27). The region on the starboard side rotates down the side of the model in the direction of spin as the spin rate increases. The small starboard disturbance developed into the asymmetric transition region viewed on the starboard side of the model in Figures 28 and 29 at spin rates of 300 and 400 rpm, respectively. This region caused the small positive "bump" in the side force data, as seen in Figure 23. The

34

Starboard View
(Right Hand Side Facing Forward)

Bottom View (Windward Side)

Figure 26a. Smoke Photographs for $\iota = 2°$,
$V/U_\infty = 0$, $R_L = 315,000$.

Starboard View
(Right Hand Side Facing Forward)

Bottom View (Windward Side)

Figure 26b. Smoke Photographs for $\iota = 2°$,
$V/U_\infty = 0.678$, $R_L = 315,000$.

Starboard View
(Right Hand Side Facing Forward)

Bottom View (Windward Side)

Figure 26c. Smoke Photographs for $\alpha = 2°$,
$V/U_\infty = 1.020$, $R_L = 315,000$.

Starboard View
(Right Hand Side Facing Forward)

Bottom View (Windward Side)

Figure 26d. Smoke Photographs for $\alpha = 2°$,
$V/U_\infty = 1.69$, $R_L = 315,000$

36
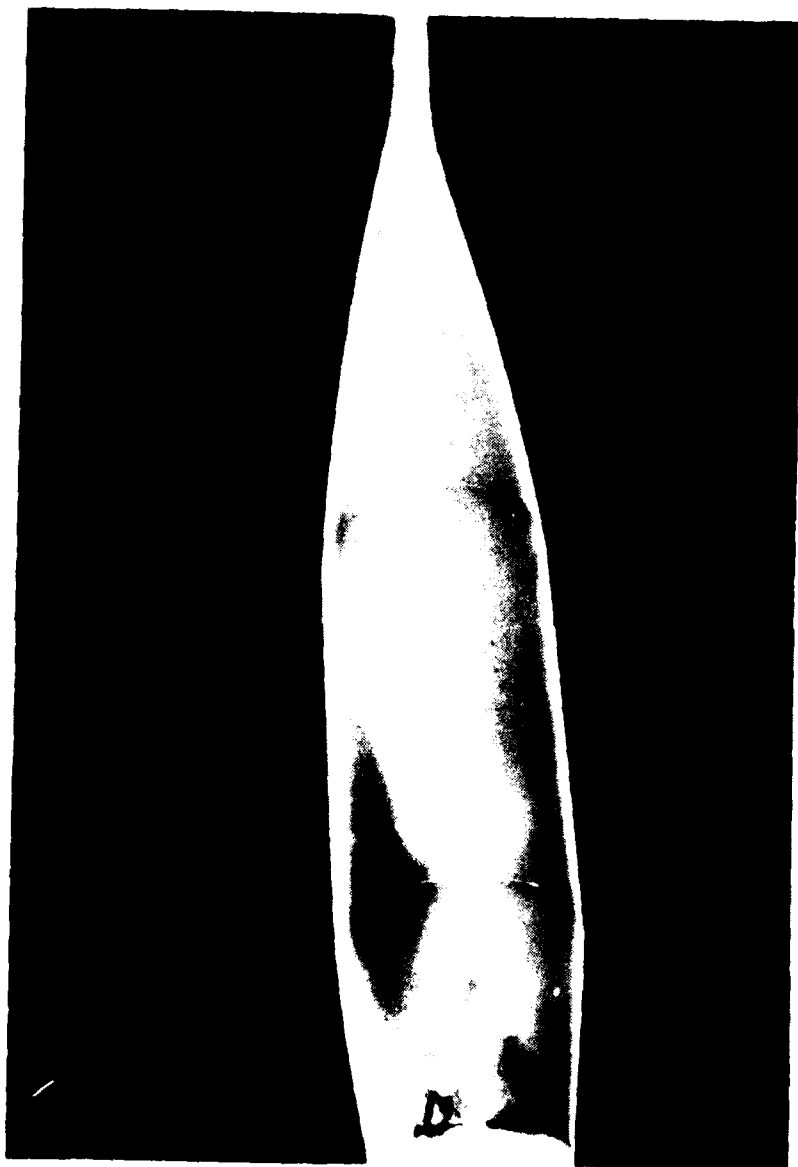
Fig. 27. Smoke Photograph for $\alpha = 4°$, $R_L = 315,000$, 0 rpm, $V/U_\infty = 0.0$ (Starboard View)
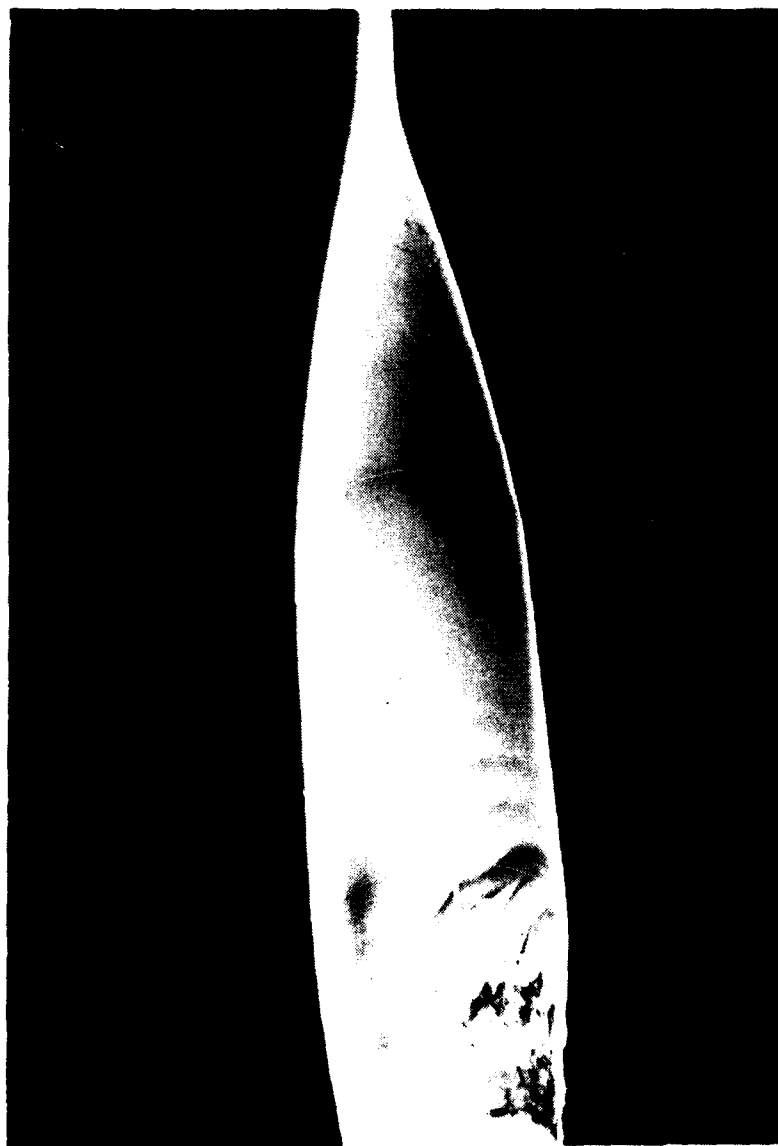
Fig. 28 . Smoke Photograph for $\alpha = 4°$, $R_L = 315,000$, 300 rpm, $V/U_\infty = 0.184$ (Starboard View)

Fig. 29. Smoke Photograph for $\alpha = 4°$, $R_L = 315,000$, 400 rpm, $V/U_\infty = 0.304$ (Starboard View)

photographs correspond to the maximum positive C_y values noted in the "bump" of the side force data. The port side is completely laminar at this spin rate, and the higher momentum transport in the transition region on the starboard side of the boattail generates a lower pressure which pulls the model in the positive C_y or negative Magnus direction. As the spin rate was increased, the asymmetric region continued to move in the spin direction around the starboard side, underneath the model (or windward side) to the port side of the model. At 750 rpm, Figure 30a shows the low frequency waves on the port side moving up on the lower rear part of the mid-section, followed by what appears to be a turbulent region on the back two-thirds of the boattail. The starboard view at 750 rpm, Figure 30b, shows the development of another mode of transition, from the cross-flow instability, that will dominate the starboard side boundary layer at all higher spin rates. Due to the turbulent region on the port side of the boattail and the transition region extending to the mid-section, the side force changes direction to the port or negative C_y side. The corresponding C_y data point in Figure 23 shows a sharp decrease in C_y at V/U_∞ equal to 0.48.

At 900 rpm the starboard view is basically unchanged from 750 rpm, with the striations moving slightly further forward on the boattail. The port view, Figure 31a, clearly shows the appearance of striations in the smoke (manifestations of the cross-flow vortices) superimposed with the now well-formed low frequency waves originating in an asymmetric transition region. It is interesting to note the difference in the angles of these two modes of transition. The striations are more closely aligned with the free stream velocity, as shown in the close-up view, Figure 31b.

At higher spin rates, the side force coefficient linearly decreases with increasing angular velocity. From 1,250 to about 2,000 rpm the starboard and port views appear to be very similar, with the exception of the low frequency waves on the port side, as displayed in Figures 32a and b at 1,500 rpm. The location and frequency of striations, the striation angle with respect to the model axis, and breakdown into turbulence appear to be identical for both views. As the spin rate was increased, both the waves and striations moved forward on the model. Additionally, at 1,500 rpm, it appeared that the striations approached an angle on the body closer to that of the waves, as shown in Figure 32c. At 2,000 rpm, a velocity ratio of 1.31, the waves no
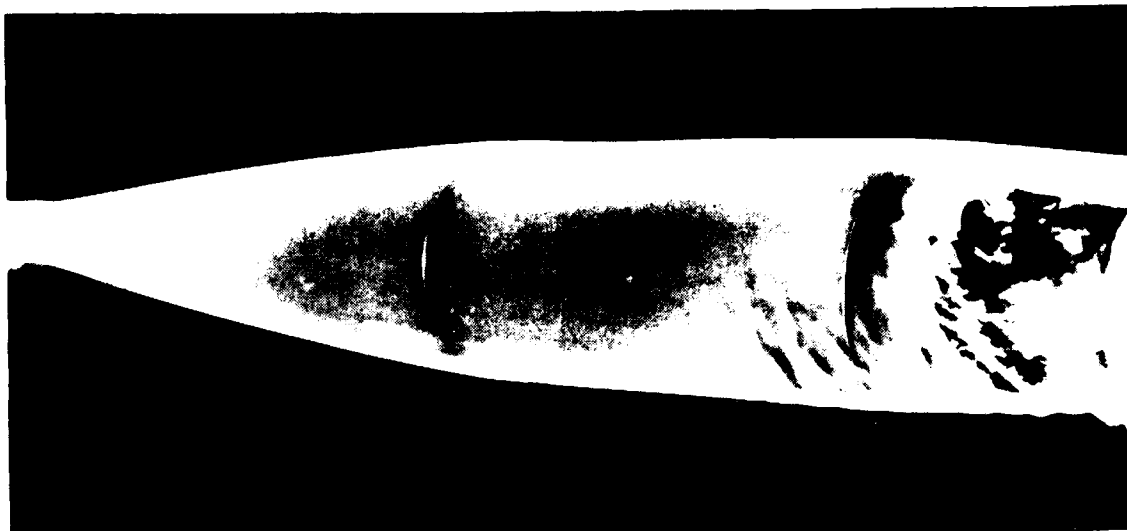
a) Port View
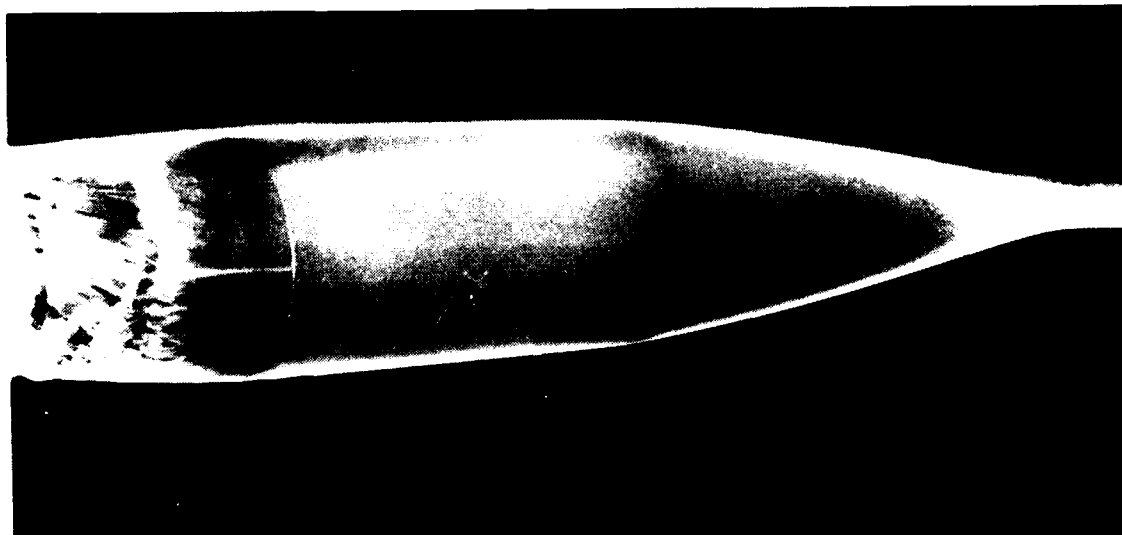
b) Starboard View

Fig. 30 . Smoke Photographs for $x = 4°$,
$R_L = 315,000$, 750 rpm, $V/U_\infty = 0.48$.

41
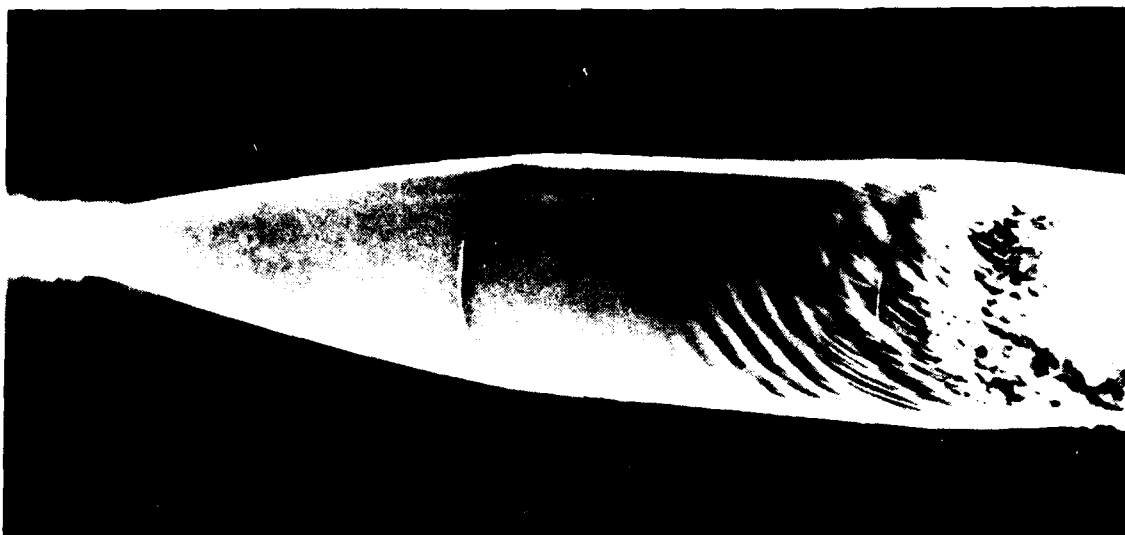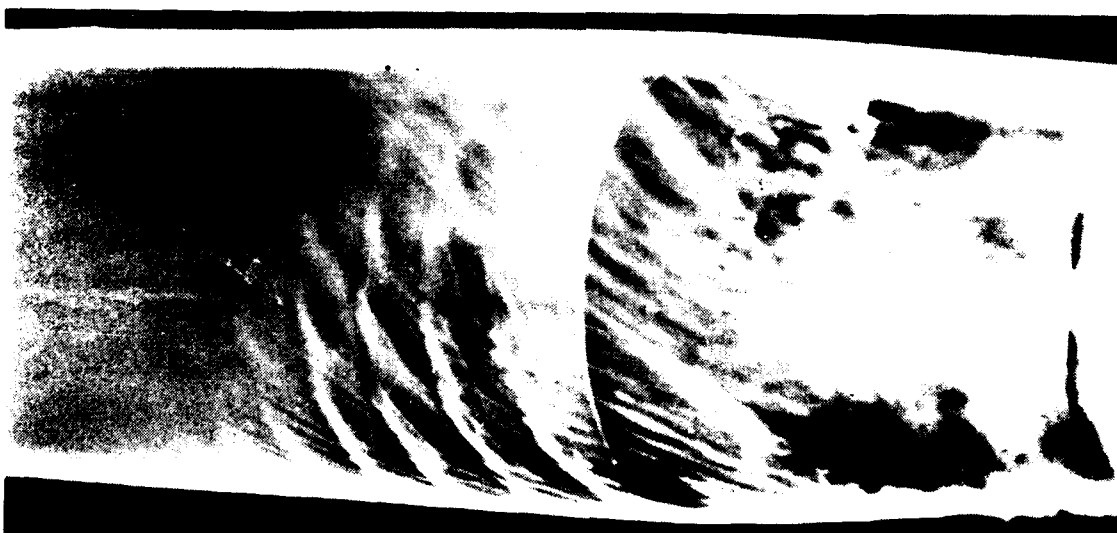
a) Port View

b) Close-up Port View

Fig. 31 . Smoke Photographs for $\alpha = 4°$,
$R_L = 315,000$, 900 rpm, $V/U_\infty = 0.56$

42
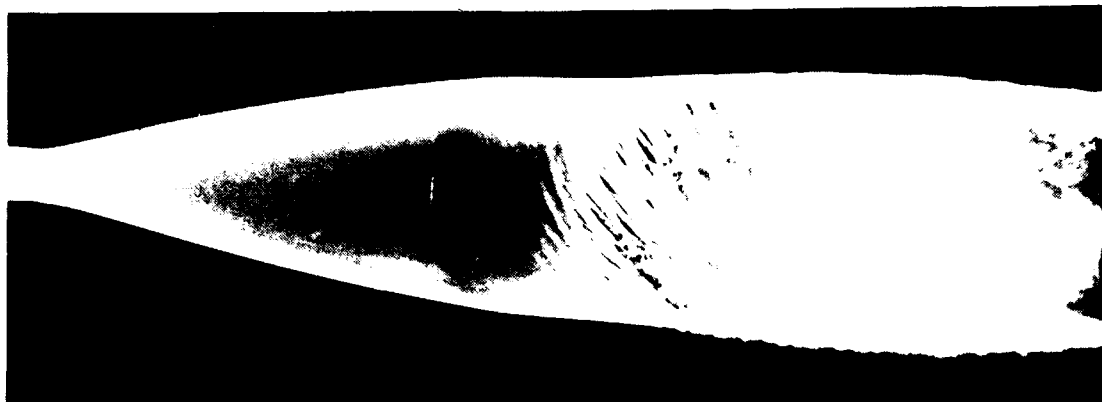
a) Port View
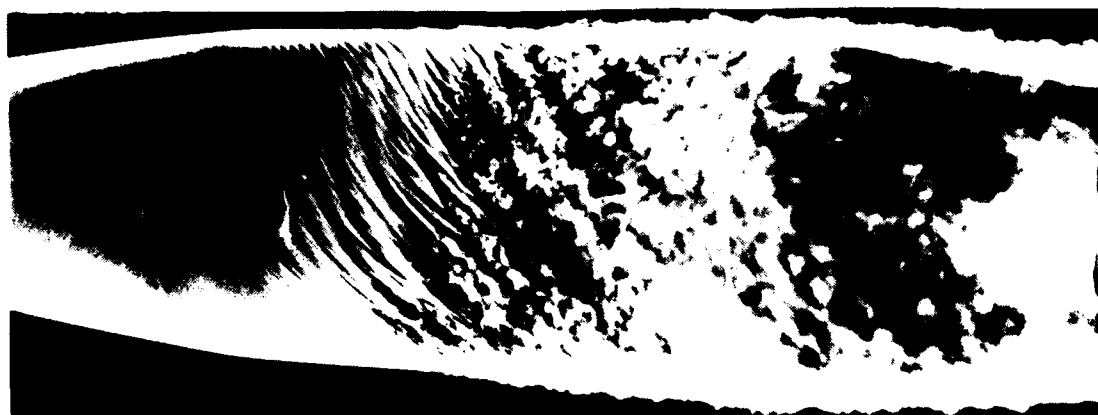
b) Starboard View

c) Close-up Port View

Fig. 32 . Smoke Photographs for $\alpha = 4°$,
R_L = 315,000, 1500 rpm, V/U_∞= 0.976.

43

longer appeared on the port side of the model, as shown in Figure 33. The starboard and port views are identical in appearance for further increases in spin rates.

Figure 34 shows a series of smoke photographs of the model at various spin rates at an angle of attack of 6° and R_L = 315,000. When the model was not spinning, the boundary layer remained attached and laminar along the entire mid-section. At a very low velocity ratio, V/U_∞ = 0.169, an asymmetric region of turbulent flow is formed on the upper rear portion of the starboard side of the model, as shown in Figure 34b. Recall that the surface velocity on the starboard side of the model opposed the cross-flow velocity; thus, the boundary layer on the starboard side was the most unstable. The first mode of transition in this unstable region resembled a two-dimensional wave, similar to that observed on the non-spinning model at zero angle of attack. The turbulent region moved slightly forward and around the model as the velocity ratio was increased to 0.339. Again, the spin rate corresponded exactly with the positive C_y "bump" in the side force versus velocity ratio curve shown in Figure 23. As the velocity ratio was increased to 0.508, the turbulent region moved entirely around the model to the windward side, as shown in Figure 34d. Also, at this spin rate, the side force coefficient had begun to decrease. The waves occurring in the first mode of transition formed at an angle that favored the cross-flow on the starboard side. However, the waves did not form at an angle equal to $\tan^{-1} V/U_\infty$. The transition region became broader and occurred more forward on the model as the velocity ratio was increased beyond 0.508. Figure 34e shows the transition process for a velocity ratio of 0.678 where striations occurring at angle of attack $\tan^{-1} V/U_\infty$ appeared superimposed over the low frequency waves. With further increases in spin rate, the turbulent region moved forward on the body, as shown in Figures 34f and g. At a velocity ratio of V/U_∞ = 1.69, the boundary layer along the entire mid-section was turbulent. Also, the Magnus force or negative side force increased linearly and the striations were visible over a shorter distance on the model, one-half caliber, as shown in Figure 34h. The turbulent zone which appeared on the leeward side and moved across the starboard side to the windward side produced a "bump" in the C_y versus V/U_∞ curve at low spin rates. At higher spin rates, the nature of the side force

44

Fig. 33. Smoke Photograph for $\alpha = 4°$, RL = 815,000, 2000 rpm, V/U = 1.31 (Close-up Port View)

Starboard View
(Right Hand Side Facing Forward)
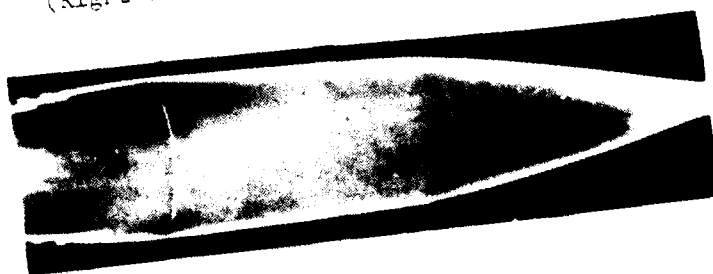
Bottom View (Windward Side)

Figure 34a. Smoke Photographs for $\alpha = 6°$,
$V/U_\infty = 0$, $R_L = 315,000$.
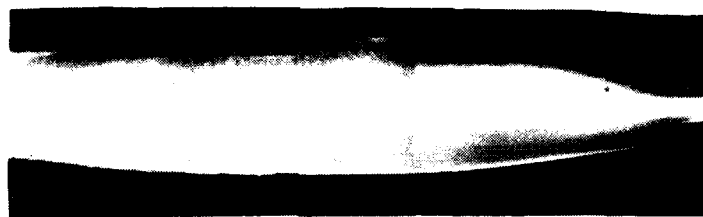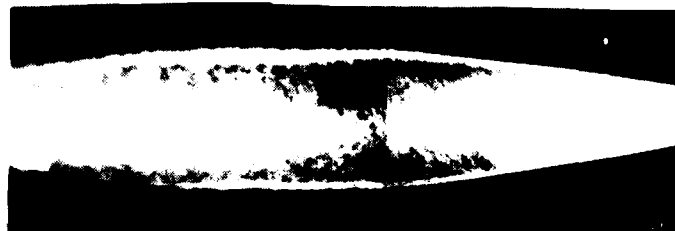

Starboard View
(Right Hand Side Facing Forward)

Bottom View (Windward Side)

Figure 34b. Smoke Photographs for $\alpha = 6°$,
$V/U_\infty = 0.169$, $R_L = 315,000$.

Starboard View
(Right Hand Side Facing Forward)

Bottom View (Windward Side)

Figure 34c.   Smoke Photographs for $\alpha = 6°$,
$V/U_\infty = 0.339$, $R_L = 315,000$.

Starboard View
(Right Hand Side Facing Forward)

Bottom View (Windward Side)

Figure 34d.   Smoke Photographs for $\alpha = 6°$,
$V/U_\infty = 0.508$, $R_L = 315,000$.

Bottom View (Windward Side)

Figure 34e. Smoke Photograph for $\alpha = 6°$, $V/U_\infty = 0.678$, RL = 315,000.

Bottom View (Windward Side)

Figure 34f. Smoke Photograph for $\alpha = 6°$, $V/U_\infty = 1.02$, RL = 315,000.
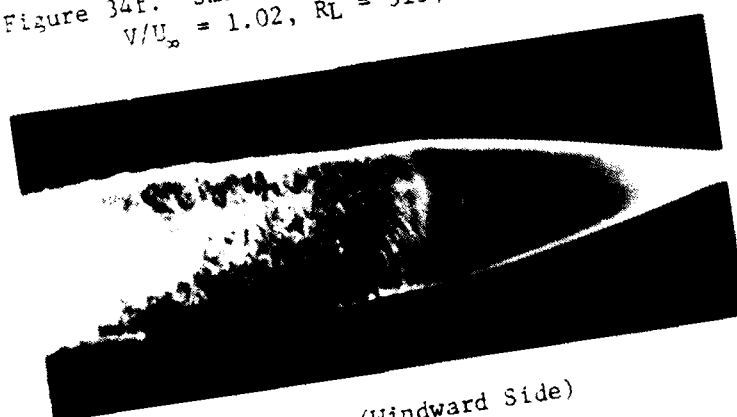
Bottom View (Windward Side)

Figure 34g. Smoke Photograph for $\alpha = 6°$, $V/U_\infty = 1.35$, RL = 315,000.

48

Starboard View
(Right Hand Side Facing Forward)

Bottom View (Windward Side)

Figure 34h. Smoke Photographs for $\alpha = 6°$,
$V/U_\infty = 1.69$, $R_L = 315,000$.

curve suggested that the classical Magnus lift was generated.

A series of smoke photographs for various spin rates at 10° angle of attack is shown in Figure 35. When the model was not spinning, a separated region appeared on the leeward side, as shown in Figure 35a. As the velocity ratio was increased to 0.85, the semi-elliptical transition region moved to the starboard side. This spin rate corresponded with the "bump" in the side force data at 10° angle of attack. The boundary layer viewed from the side appeared grossly asymmetric about the plane of angle of attack. At the lower angles of attack, striations form at the striation angle $\tan^{-1} V/U_\infty$, regardless of spin rate. The side force decreased with further increases in spin rate as expected. Figure 35c shows the boundary layer transition for a velocity ratio of 1.02 where the "bump" in the Magnus force diminished. The boundary layer, as viewed from the windward side, still appeared asymmetric although not as asymmetric as at $V/U_\infty = 0.85$.

The boundary layer for a velocity ratio of 1.69 is shown in Figure 35d. The transition region occurred symmetrically about the plane of angle of attack. Furthermore, a positive Magnus force was induced on the model at this spin rate. Obviously, the cross-flow component of velocity was greatest at 10° angle of attack. Apparently, there was enough vorticity shed into the flow to produce a positive Magnus lift. Up to a velocity ratio of 1.02 there was a combination of the classical Magnus lift with a negative Magnus lift generated by asymmetric transition. Beyond this range the Magnus force increased linearly with increasing spin rate. The side force versus velocity ratio curves for 8° and 10° are similar and it may be inferred that the same mechanisms are active at 8° angle of attack.

As already shown in Figure 24, the increased cross-flow velocity component at higher angles of attack affected the shape, size and location of the asymmetric transition region at a given flow velocity and spin rate. With increasing angle of attack, the transition region covered a larger portion of the starboard side and began earlier or further upstream on the model mid-section. Also, due to the increased cross-flow velocity component opposing the rotation of the starboard surface of the model, the asymmetric transition region was higher on the starboard side with each incremental increase in angle of attack.

Starboard View
(Right Hand Side Facing Forward)
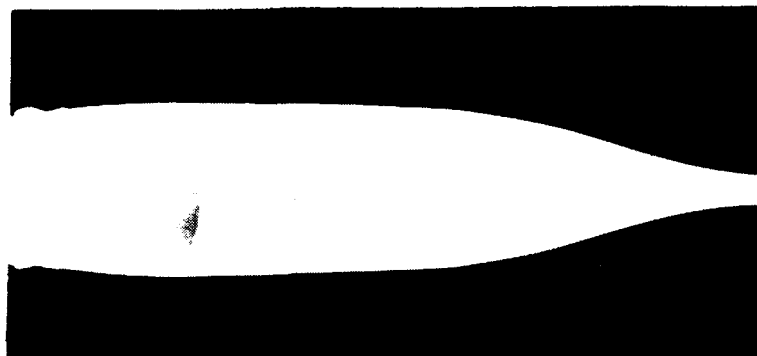
Bottom View (Windward Side)

Figure 35a. Smoke Photographs for $x = 10°$,
$V/U_\infty = 0$, $R_L = 315,000$.

Starboard View
(Right Hand Side Facing Forward)

Figure 35b. Smoke Photograph for $x = 10°$,
$V/U_\infty = 0.35$, $R_L = 315,000$.

53

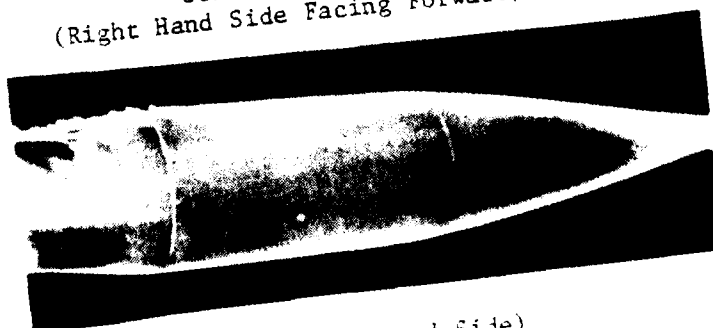Starboard View
(Right Hand Side Facing Forward)

Bottom View (Windward Side)

Figure 35c.   Smoke Photographs for $\alpha = 10°$,
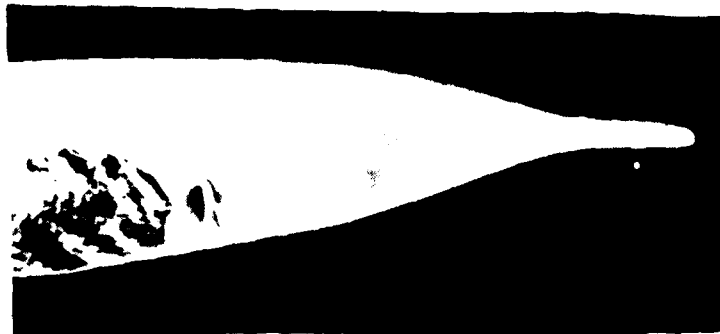$V/U_\infty = 1.020$, $R_L = 315,000$.
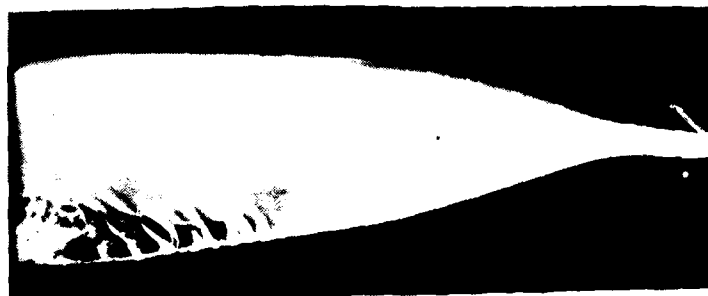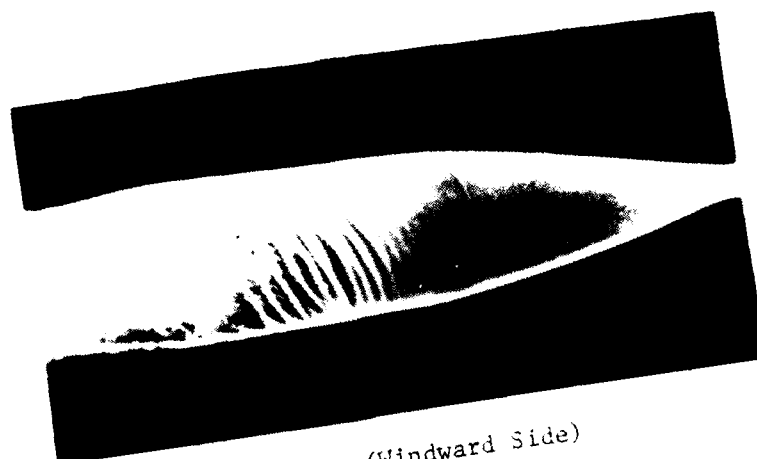

Starboard View
(Right Hand Side Facing Forward)

Bottom View (Windward Side)

Figure 35d.   Smoke Photographs for $\alpha = 10°$,
$V/U_\infty = 1.69$, $R_L = 315,000$.

Noticeable angle of attack effects were evident for higher spin rates where the asymmetric transition region had rotated in the direction of spin down and under the starboard side. Figure 36 displays the effect of angle of attack for the Reynolds number of 315,000 and a spin rate of 1,500 rpm for a velocity ratio equal to 1.02. Figures 36a, b and c for 2°, 4° and 6° angle of attack interestingly show the initial development of the spin-induced striations occurring just behind the nose/mid-body juncture for all cases, yet show a transition to turbulence that takes much longer and occurs much later on the model's mid-section with each increase in angle of attack. The striations break down almost immediately into turbulence about one-third the distance along the mid-section for 2°, yet do not undergo transition until just before one-half and at about two-thirds the mid-section distance for 4° and 6°, respectively. Figures 36d and e at 8° and 10° display the simultaneous occurrence of these striations and the low frequency waves on the windward side of the model. Consistent with earlier observations, the low frequency disturbances appear higher on the model's starboard side for 10°. Initial striation development occurs once again just behind the mid-section juncture, but the additional presence of the low frequency waves seems to effect an earlier transition to turbulence than for 6°, particularly on the windward half of the model's mid-section. Striation breakdown and transition to turbulence, independent of the low frequency disturbances, still occur on the leeward half of the model behind the transition location in the 4° case.

Figure 37, at the same Reynolds number (315,000), exhibits an identical trend as the previous angle of attack sequence for a spin rate of 2,500 rpm. Initial striation development occurs on the model nose for all cases, but transition to turbulence moves downstream and occurs closer to the nose/mid-body intersection with each subsequent increase in angle of attack. The low frequency waves are visible on the windward side of the model only at 10°.

The effect of increasing angle of attack is also evident in the boundary layer of the non-spinning model. Figures 38a, b, c and d for the low Reynolds number at 4°, 6°, 8° and 10°, respectively, display increasing areas of transition and turbulence with increasing angle of attack. The boundary layers are similar for 4° and 6°, with laminar flow present on the entire

a) $\alpha = 2°$
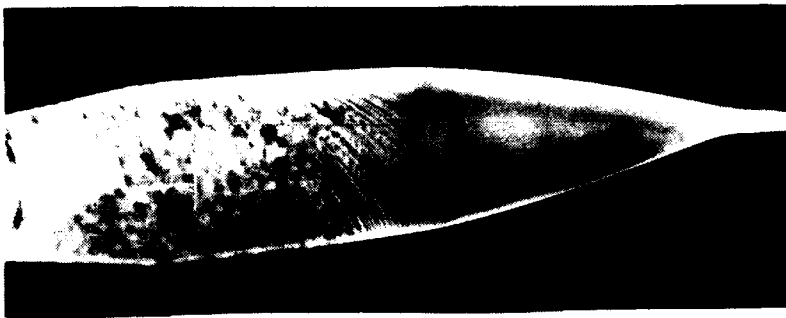
b) $\alpha = 4°$
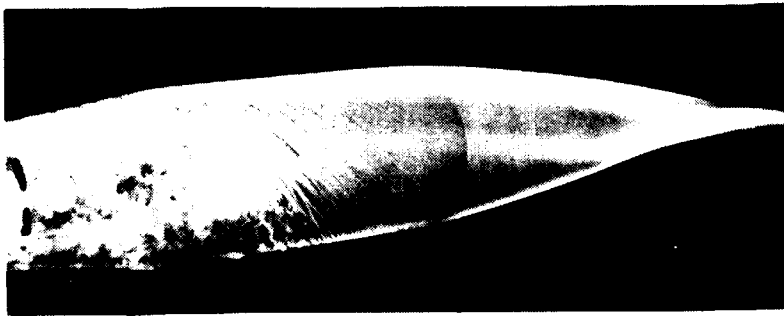
c) $\alpha = 6°$

Figure 36.   Smoke Visualization of Angle of Attack Effect at a
Camera Axis 55° from Flow Direction Facing Upstream for:
R_L (Sharp Nose) = 315,000, 1500 rpm, V/U_∞= 1.02
(Starboard View)
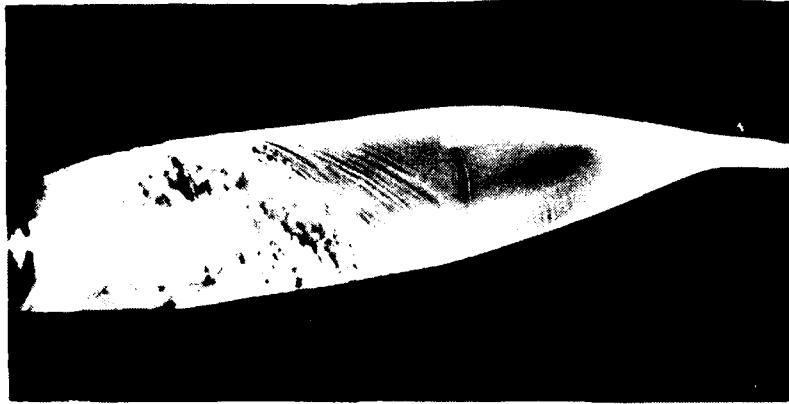
d) $\alpha = 8°$
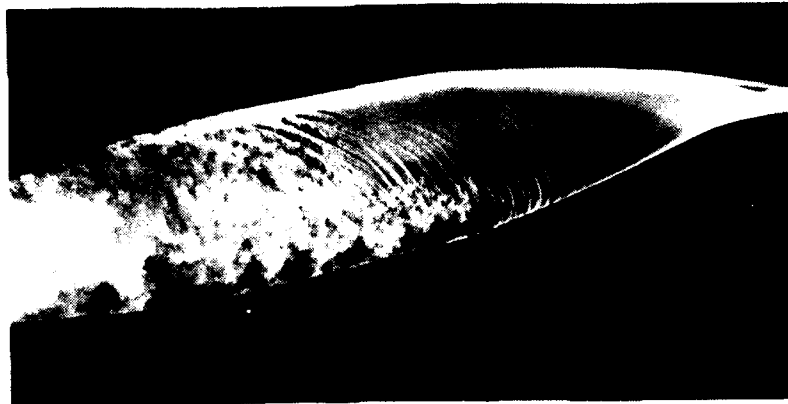
e) $\alpha = 10°$

Figure 36 (Cont.) Smoke Visualization of Angle of Attack Effect at a
Camera Axis 55° from Flow Direction Facing Upstream for:
R_L (Sharp Nose) = 315,000, 1500 rpm, V/U_∞= 1.02
(Starboard View)

a) $\alpha = 2°$
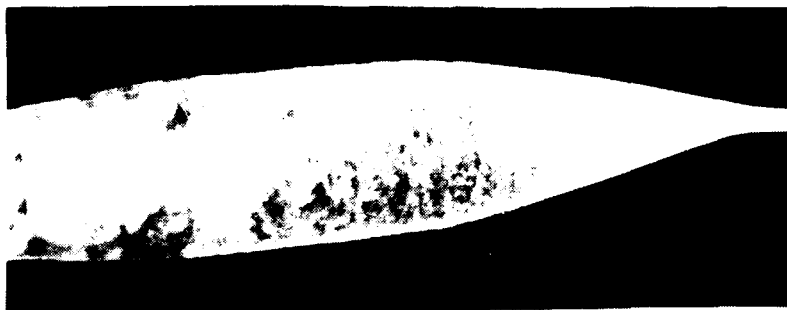
b) $\alpha = 4°$

c) $\alpha = 6°$

Figure 37. Smoke Visualization of Angle of Attack Effect at a
Camera Axis 55° from Flow Direction Facing Upstream for:
R_L (Sharp Nose) = 315,000, 2500 rpm, V/U_∞= 1.64
(Starboard View)

d) $\alpha = 8°$
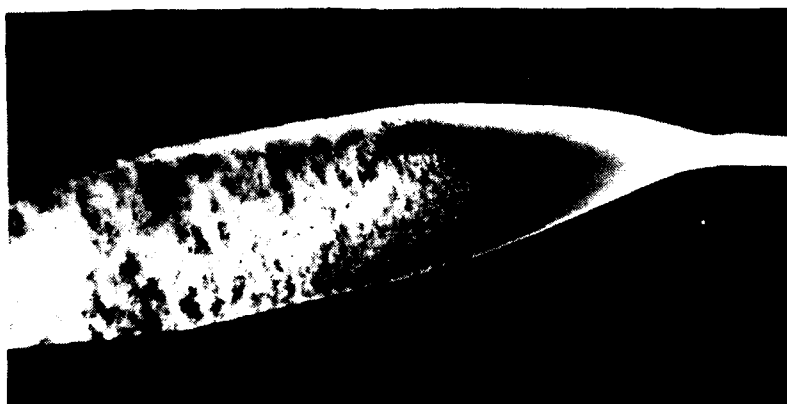
e) $\alpha = 10°$

Figure 37 (Cont.) Smoke Visualization of Angle of Attack Effect at a
Camera Axis 55° from Flow Direction Facing Upstream for:
R_L (Sharp Nose) = 315,000, 2500 rpm, $V/U_\infty = 1.64$
(Starboard View)
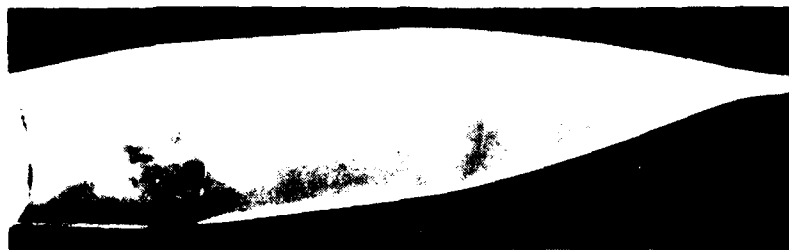
a) $\alpha = 4°$
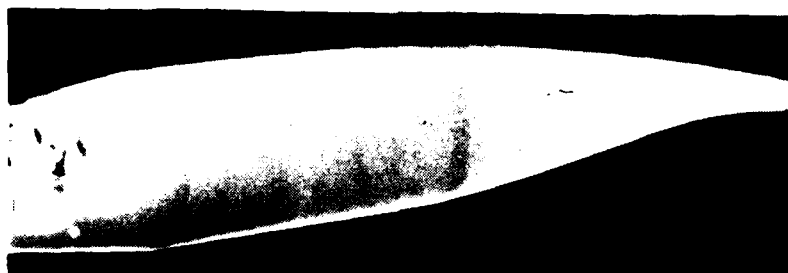
b) $\alpha = 6°$
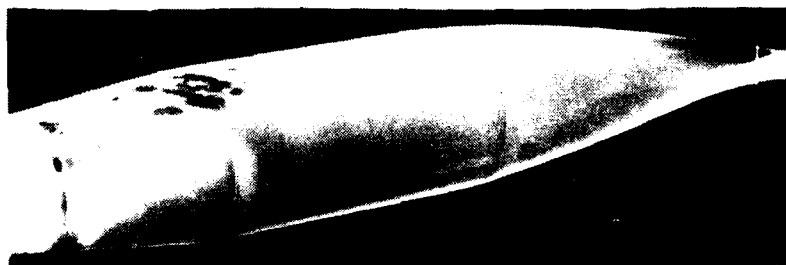
c) $\alpha = 8°$

d) $\alpha = 10°$

Figure 38. Smoke Visualization of Angle of Attack Effect at a
Camera Axis 55° from Flow Direction Facing Upstream for:
R_L (Sharp Nose) = 315,000, 0 rpm, $V/U_\infty = 0.0$
(Starboard View)

58

model, with the exception of a small turbulent region on both sides of the rear section of the boattail. As the 0° and 2° non-spinning cases exhibit complete laminar flow over the entire body, these turbulent regions later develop into the aforementioned asymmetric transition regions caused by spinning. The turbulent region at 6° angle of attack is slightly larger than at 4°, and extends slightly further upstream on the boattail. The turbulent boundary layer regions in the 8° and 10° cases, displayed in Figures 38c and d, are markedly different in size, description and location from the lower angles of attack. The turbulent region has moved to the leeward side of the model and extends about mid-way up the model mid-section. The boundary layer for 10° appears to extend just slightly further upstream on the mid-section and may be more turbulent.

INFLUENCE OF NOSE BLUNTNESS

The investigation on the effect of nose bluntness was carried out in two experimental phases.[35] First, a visual study was conducted at zero angle of attack for both the spinning and non-spinning cases. Test Reynolds numbers (based on the sharp-nosed model length) between 315,000 and 1,030,000 were used. The second phase involved the measuring of the Magnus forces on the spinning models at angles of attack up to 10°. Still smoke photographs were taken at these angles of attack to obtain visual data for correlation with the side force observations. The baseline sharp-nosed model was used, together with all three spherically-blunted noses in all phases of the investigation.

Spinning and Non-Spinning Model at Zero Angle of Attack - Smoke Visualization

Before investigating the effects of nose bluntness at angle of attack, the initial phase attempted to recognize trends in the boundary layer development and transition at a given free stream velocity and spin rate as the nose bluntness was increased. Photographs were taken at Reynolds numbers (based on the sharp nosed model length) of 315,000, 608,000, 860,000, 928,000 and 1,030,000, with spin rates of 0, 500, 1,500, 2,500 and 4,000 rpm.

Figures 39a, b, c and d display the effects of bluntness on the flow characteristics for the non-spinning case at a Reynolds number (based on the

a) Sharp Secant Ogive Nose
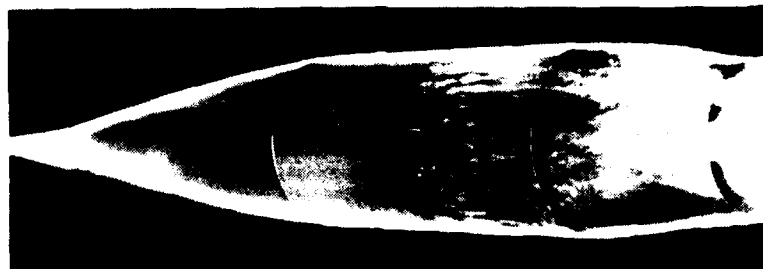
b) 10% Bluntness Ratio Nose

c) 20% Bluntness Ratio Nose

d) 30% Bluntness Ratio Nose

Figure 39. Smoke Visualization of Bluntness Effect at a
Camera Axis 55° from Flow Direction Facing Upstream for:
R_L (Sharp Nose) = 1,030,000, 0 rpm, $\alpha = 0°$
(Port View)

sharp nosed model length) of 1,030,000. In going from the sharp to 10%
blunt nose, there is a marked difference in the Tollmien-Schlichting waves
and three-dimensional truss (i.e., vortex loop) formation and location.
The Tollmien-Schlichting waves appear slightly further forward on the mid-
section of the 10% nose, as well as being of slightly higher frequency than
on the sharp nose. The trusses on the sharp nose begin to appear at about two-
thirds of the distance along the mid-section, while, on the 10% nose, they
appear at about one-half of the distance along the mid-section. The sharp
nosed trusses are sharp and elongated in addition to being staggered row by
row, while the 10% nose shows three rows of shorter and wider aligned trusses
followed by two longer staggered rows. Since these trusses break down
immediately into turbulence, this change may indicate some difference in the
formation of the turbulent boundary layer. Increasing bluntness from 10%
to 20%, the Tollmien-Schlichting waves appear in about the same location
for both cases but there seem to be fewer rows of trusses (i.e., one or two)
before an earlier breakdown into turbulence for the 20% nose. Flow conditions
for the 30% nose seem to be very similar in description but transition from
Tollmien-Schlichting wave to vortex loop appears to occur just slightly
later.

Figures 40a, b, c and d, at a Reynolds number of 928,000 and spin rate
of 1,500 rpm, simultaneously show the occurrence of both Tollmien-Schlichting
waves and cross-flow vortices. In going from sharp to 10% nose bluntness,
the Tollmien-Schlichting waves are much more clearly defined in the 10%
bluntness case, being barely visible on the sharp nose. The smoke striations
from the cross-flow vortices become helical further upstream on the 10% blunt
nose and break down into turbulence further back on the boattail than or the
sharp nose. The 10% and 20% nose bluntness cases appear to be similar in
individual events, with the possible exception that they all occur slightly
further upstream for the 20% blunt nose. For the 30% blunt nose, the
striations break down immediately into turbulence at about two-thirds of the
distance along the mid-section. For all other noses, turbulence was not
developed until back on the boattail.

Figures 41a, b, c and d display the effect of bluntness at a higher
velocity ratio equal to 0.654 for a Reynolds number of 860,000 at 2,500 rpm.
At this lower Reynolds number, only the cross-flow induced striations are

a) Sharp Secant Ogive Nose
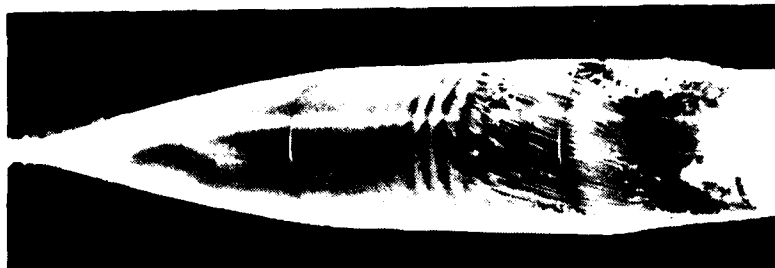
b) 10% Bluntness Ratio Nose
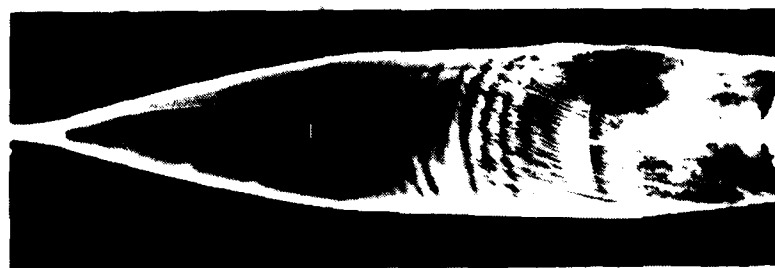
c) 20% Bluntness Ratio Nose
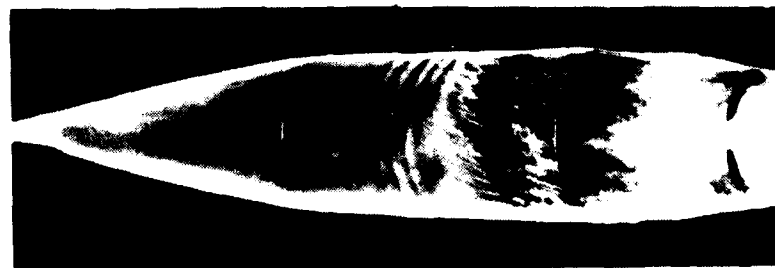
d) 30% Bluntness Ratio Nose

Fig. 40. Smoke Visualization Photographic Sequence at a
Camera Axis 55° from Flow Direction Facing Upstream for:
R_L (Sharp Nose) = 928,000, 1500 rpm, $\alpha = 0°$.
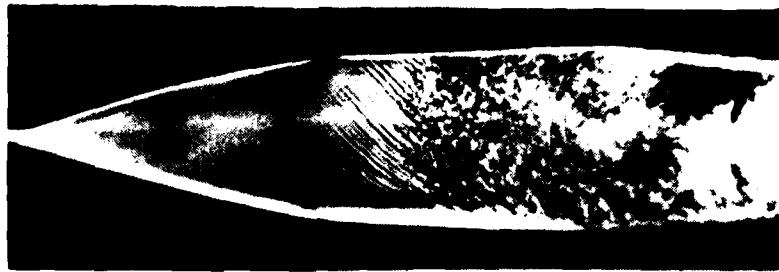
a)   Sharp Secant Ogive Nose
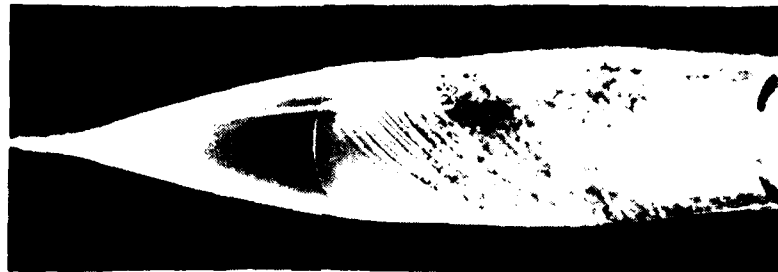
b)   10% Bluntness Ratio Nose
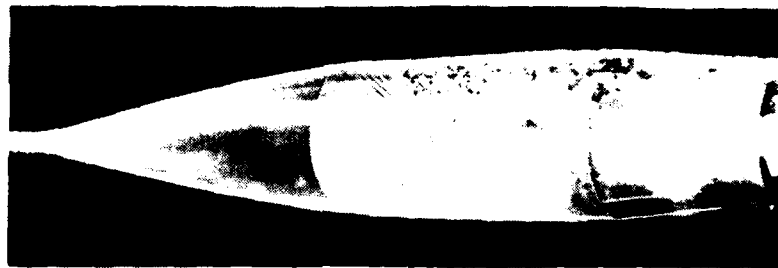
c)   20% Bluntness Ratio Nose
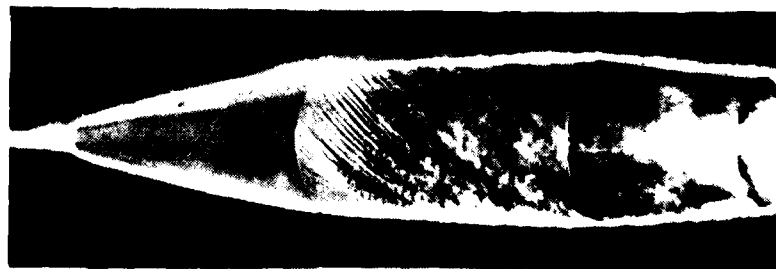
d)   30% Bluntness Ratio Nose

Figure 41.   Smoke Visualization of Bluntness Effect at a
Camera Axis 55° from Flow Direction Facing Upstream for:
RL (Sharp Nose) = 360,000, 2500 rpm, $\iota = 0°$
(Port View)

visible as transition phenomena. With increasing bluntness, the location of both striation formation and breakdown to turbulence has moved forward. As shown in the previous and following sequences, this simple relationship does not apply for all noses in most increasing bluntness progressions.

An effect of bluntness sequence at a sharp-nosed Reynolds number of 1,030,000 and spin rate of 1,500 rpm displayed a different trend. The peripheral to free stream velocity ratio (V/U_∞), held constant for the three noses, was equal to 0.33. There was a marked difference in the location and formation of both boundary layer instabilities visible between the 10% bluntness ratio nose and the 20% nose. The two-dimensional Tollmien-Schlichting waves appeared to form further forward on the mid-section of the 20% nose than for the 10% nose. The spin-induced striations on the 10% nose began to form at about one-half the distance back on the boattail and broke down into turbulence at three-fourths the mid-section body length. These locations differed greatly from those of the same occurrences on the 20% nose where the striations formed at one-third the mid-section and broke down into turbulence at one-half the distance back along the mid-section. The 30% case appeared to closely resemble the 20% nose phenomenon, with the exception of the striation breakdown to turbulence location. Transition appeared to occur slightly further back on the mid-section than for the 20% case yet still ahead of the transition location for the 10% nose.

A similar trend was exhibited for the non-spinning case at a sharp-nosed Reynolds number of 928,000. Tollmien-Schlichting waves first occurred on the 10% nose at a point one-third of the distance along the mid-section, and transition into three-dimensional vortex trusses at about seven-eighths the mid-section length. Turbulence occurred just behind the mid-section/boattail juncture. The locations of all boundary layer developments occurred further upstream for the 20% nose model than for the 10%. Tollmien-Schlichting waves were visible starting at one-fourth the mid-section length, with trusses occurring at two-thirds the distance along the mid-section. The turbulent boundary layer appeared just before the boattail. The behavior of the 30% nose boundary layer closely resembled that of the 20% nose but, once again, as in the previous sequence of pictures, transition to turbulence occurred later on the 30% model than on the 20% nose model. In addition, the location of the initial Tollmien-Schlichting wave and the three-dimensional trusses

64

appear to have moved back slightly along the mid-section.

For a Reynolds number of 928,000 and at a 2,500 rpm spin rate, V/U_{∞} equal to 0.585, faint Tollmien-Schlichting waves were visible on the 10% nose at about one-third the distance along the mid-section body and were superimposed with striations which changed to turbulence at mid-section. For the 20% nose, the first Tollmien-Schliching waves appeared to have moved upstream to a point about one-fourth the distance back along the mid-section. The cross-flow vortices also seemed to have developed earlier in the flow and appeared to be of a slightly higher frequency than the striations of the 10% nose. The turbulent region covered approximately 60% of the mid-section for the 20% case, compared to only half of the 10% bluntness case. Flow conditions for the 30% nose seemed to be similar in location and description to the 20% nose.

All the above cases demonstrated the trend of earlier boundary layer transition development, with increasing bluntness from the sharp nose. Increasing bluntness from the sharp nose through the 20% bluntness ratio nose demonstrated that most (but not all) boundary layer transition phenomena seemed to occur earlier or formed further upstream on the model. This effect of bluntness on the boundary layer was observed in the location of the two-dimensional Tollmien-Schlichting wave formation, the transition to three-dimensional trusses and the subsequent breakdown to turbulence, as well as the location of the formation of the cross-flow induced vortices or striations and their transition to turbulence. In some cases, an increase in bluntness resulted in an increase in the striation frequency or caused a clearer definition of the two-dimensional Tollmien-Schlichting waves, but no particular trend was apparent. No consistent trend described the behavior of increasing bluntness from one nose to the next in all bluntness sequences. An example of this disparity is evidenced in examining the above bluntness sequence descriptions and Figures 39 through 41, where the 20% to 30% increase in nose bluntness resulted in both earlier and later boundary layer transition phenomena. It is interesting to note that no significant bluntness effects were observed in the boundary layer development at the lower Reynolds numbers of 315,000 and 608,000 or at the highest spin rate of 4,000 rpm for this zero angle of attack investigation.

65

Spinning Model at Angle of Attack - Side Force Measurements

Magnus force measurements were made using all four noses at Reynolds numbers of 315,000 and 1,030,000, based on total model length. Since the blunt nosed axisymmetric models were actually shorter than the sharp-nosed baseline version, the tunnel velocity was increased slightly to keep the Reynolds number constant for all tests. Side forces generated from the spinning model were measured at angles of attack of 2°, 4°, 6°, 8° and 10° for both Reynolds numbers at spin rates of up to 6,000 rpm. This spin rate corresponds to peripheral-to-free-stream-velocity ratios, V/U_∞, of 3.9 and 1.17 for the low and high Reynolds number cases, respectively, for the sharp-nosed model. Maximum velocity ratios were slightly lower for the blunt-nosed models, due to the slightly higher free stream velocities of these test cases. The side force data were reduced and plotted in non-dimensional form as C_y versus velocity ratio.

Figures 42 and 43 compare the side force data for the sharp nose and the three spherically-blunted noses at the particular angles of attack of 8° and 10°, respectively, for the low Reynolds number case. Although the patterns of the individual data for each nose are similar, the magnitude of the side force coefficient groups the data for the sharp and 30% bluntness ratio noses together, as well as the data for the 10% and 20% bluntness ratio noses. Since the forces generated at this low Reynolds number case are so small (as low as $\simeq 0.01$ Newton) conclusions cannot be drawn at this time as to the effect of nose bluntness on the Magnus force for the low Reynolds number case. However, the nature of the data and the trends established are supported by the visualization data. The fabrication of a more sensitive and stable strain gauge amplifier is nearing completion and this should yield additional data at the low Reynolds case in the near future.

The side force coefficients measured for the high Reynolds number, 1,030,000, were generally of a much smaller magnitude than the low Reynolds number values for a particular angle of attack. Figures 44 through 47 show the side force characteristics of the four noses at angles of attack of 4°, 6°, 8° and 10°, respectively. It should be pointed out that the smaller non-dimensional C_y values at the high Reynolds number do not indicate that the actual side forces generated were smaller. The maximum side force

Figure 42. Side Force versus Velocity Ratio for
α = 8° and R_L (Sharp Nose) = 315,000
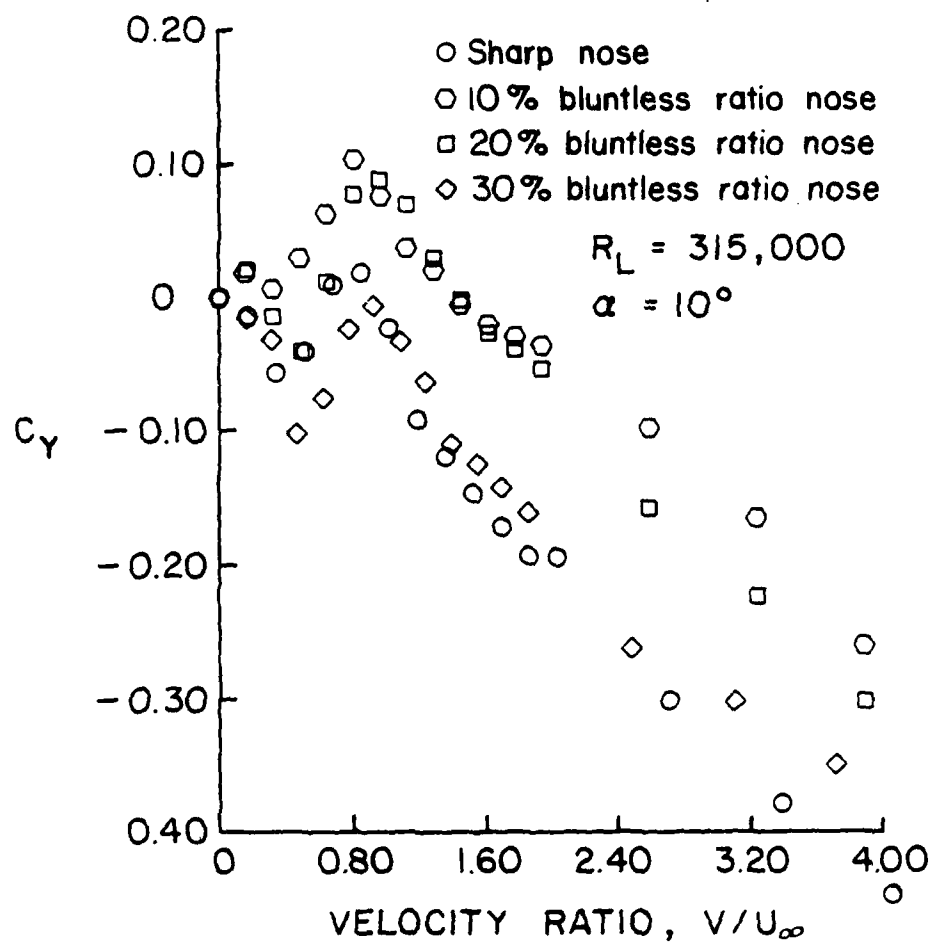
Figure 43.   Side Force versus Velocity Ratio for
$\alpha = 10°$ and R_L (Sharp Nose) = 315,000

measured at the high Reynolds number case was about twice that of the low Reynolds number case. However, the force measured at the high Reynolds number was divided by a much higher dynamic pressure, q, to arrive at the side force coefficient.

Figure 44, for an angle of attack of 4°, shows a clustering of points around the zero C_y value throughout the spin rate range. All curves show a gradual increase in C_y up to a maximum value of about +0.025 at a velocity ratio of 0.5, and then leveling off along the zero C_y axis. Increasing the angle of attack tended to displace the individual curves with respect to the C_y axis.

The 6° angle of attack data are presented in Figure 45. The sharp nosed model had the highest C_y at most velocity ratios, with the noses of increasing bluntness having greater Magnus forces. The side force data for the 30% blunt nose falls below the zero C_y axis before increasing to its maximum value at a velocity ratio of approximately 0.6. This trend is the initial occurrence of the side force "bucket" in the negative C_y direction, which dominates the data for all noses at higher angles of attack.

At 8° angle of attack, Figure 46, the "bucket" in the side force coefficient data is more evident with the 20% and 30% blunt noses. For these noses, a maximum negative C_y of −0.046 was obtained at a velocity ratio of about 0.36. After the maximum negative C_y has been reached, the side force coefficient increases positively for all noses and attains a maximum at a velocity ratio equal to 0.64.

Figure 47, the side force data for the four noses at 10° angle of attack, displays several trends observed in the three previous figures. First, the negative side force "bucket" has continued to deepen, with the 20% and 30% bluntness ratio noses once again showing the most negative C_y. The curve for the 20% bluntness ratio nose reaches a minimum C_y of −0.115 at a velocity ratio of about 0.35, approximately the same spin rate at which the 6° and 8° cases displayed their minimum C_y values. Additionally, the velocity ratio at which the individual curves reach their maximum positive values of C_y increases with increasing angle of attack. This movement of the positive C_y peak was observed in the low Reynolds number data. In both cases, the maximum side force coefficient seemed to occur at a slightly higher velocity ratio value with increased angle of attack. It is interesting to note that,

69
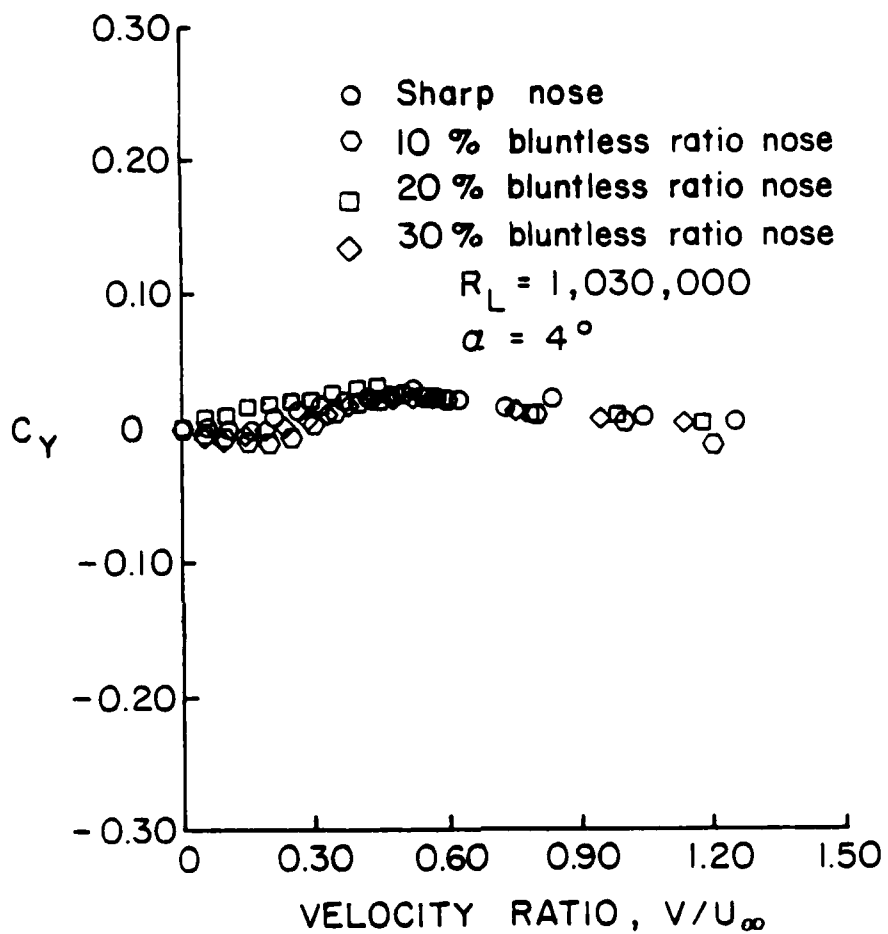
Figure 44. Side Force versus Velocity Ratio for
$\alpha = 4°$ and R_L (Sharp Nose) = 1,030,000

70
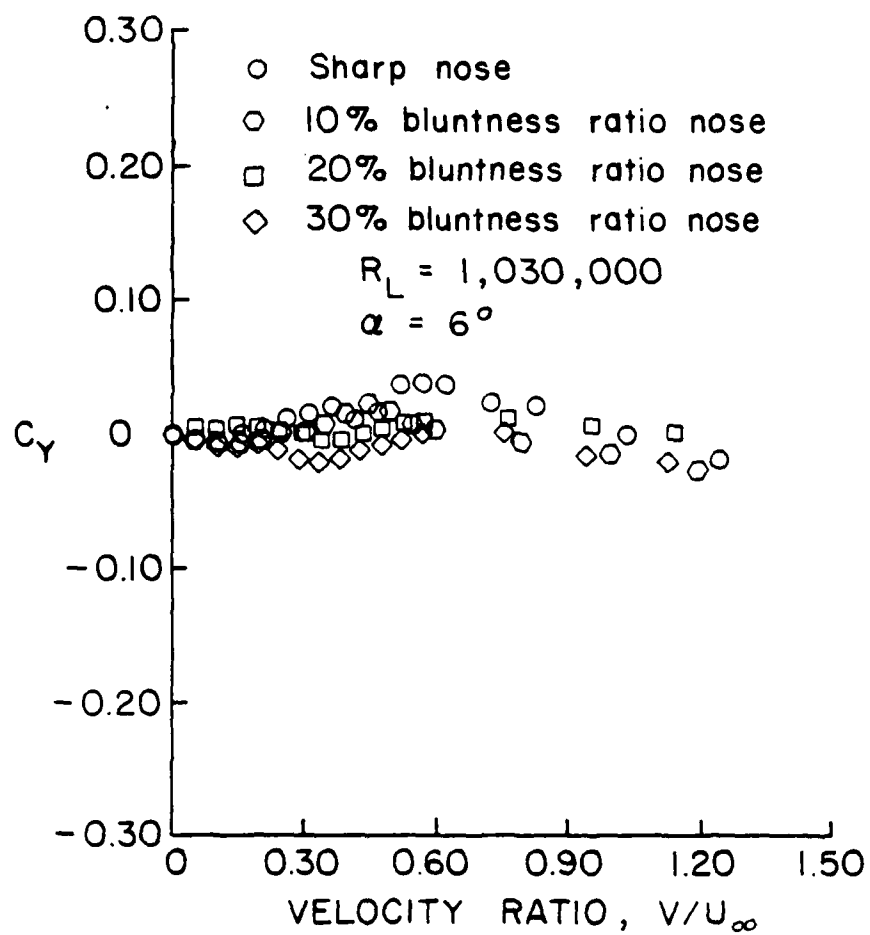
Figure 45. Side Force versus Velocity Ratio for
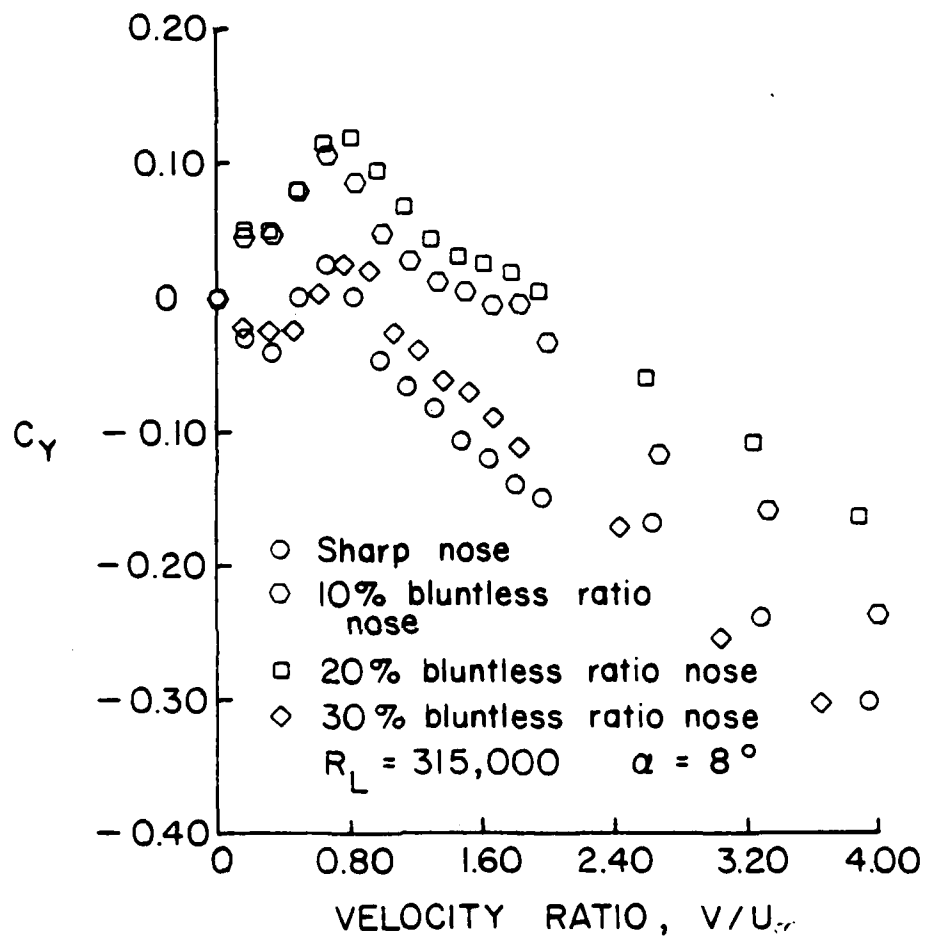$\alpha = 6°$ and R_L (Sharp Nose) = 1,030,000

71
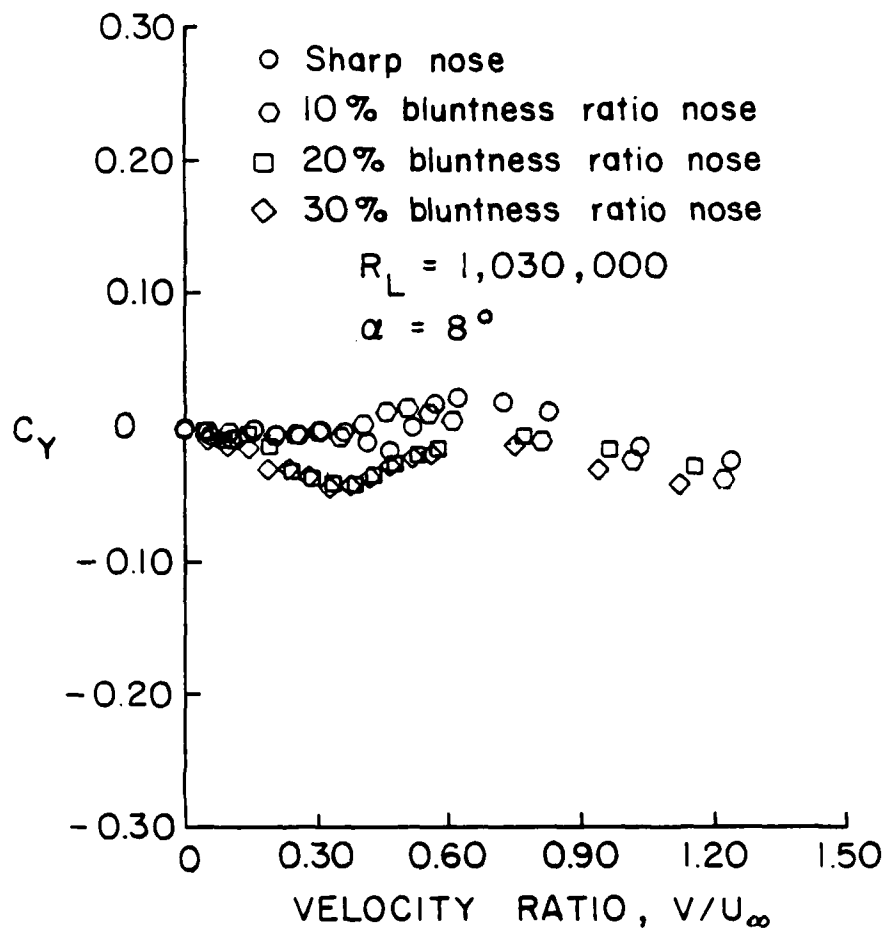
Figure 46. Side Force versus Velocity Ratio for
$\alpha = 8°$ and R_L (Sharp Nose) = 1,030,000
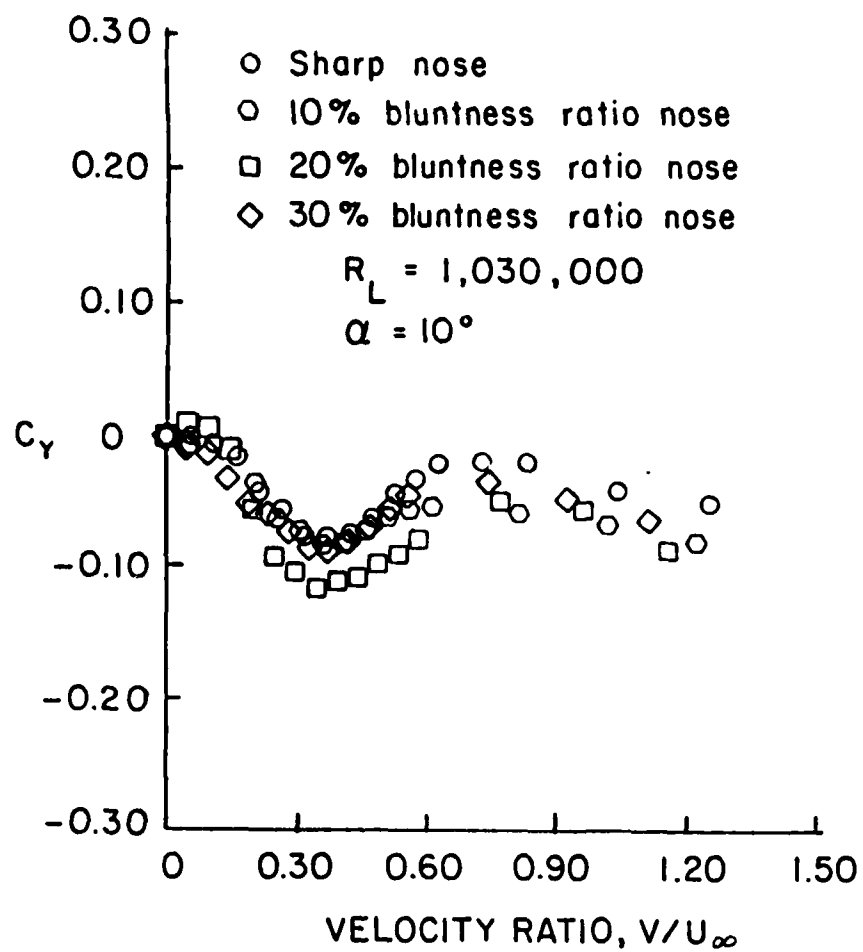
Figure 47. Side Force versus Velocity Ratio for
$\alpha = 10°$ and R_L (Sharp Nose) = 1,030,000.

although the C_y peaks occur between 500 and 1,250 rpm for the low Reynolds number data, the velocity ratio values at the C_y peak are quite similar for low and high Reynolds number cases at a given angle of attack. At a Reynolds number of 315,000, V/U_∞ at C_y maximum equals 0.66 and 0.74 at 8° and 10°, respectively. For the high Reynolds number case, 1,030,000, V/U_∞ at C_y maximum equals 0.64 and 0.68 at 8° and 10°. From these observations and from a comparison of the C_y values of the high and low Reynolds numbers for a given nose geometry, angle of attack, and velocity ratio, it is clear that the shape of the curves is similar, as shown previously in Figure 25. This suggests that neither the free stream velocity nor the spin rate alone are the important parameters affecting boundary layer development and Magnus force, but their ratio, V/U_∞, affects these phenomena to a large extent.

Smoke Photographs

Photographs were taken at the appropriate Reynolds number and spin rate which corresponded exactly with the side force data for the sharp nosed model. Note that the length of the models decreases slightly as the bluntness ratio is increased. Photographs of the blunt noses were taken at the same free stream velocity and spin rates as the sharp-nosed models and, therefore, R_L is slightly lower in the blunt nose photographs.

Pictures were taken at all angles of attack for the sharp nose for both Reynolds numbers throughout the range of spin rates from zero to 5,000 rpm. Smoke photographs were taken of the blunted noses only for those cases where differences in the boundary layer transition region, due to nose geometry, were observed, as suggested by the side force data. These differences were noted at higher angles of attack for both Reynolds numbers.

Several series of smoke photographs were taken at higher angles of attack to document effects of nose bluntness. Photographs were taken at flow conditions where differences in side force curves had been observed, as discussed earlier. Nose bluntness sequences were taken at 8° and 10° for the low Reynolds number of 315,000, and at 10° for a Reynolds number of 1,030,000. Spin rates ranged from zero to 2,500 rpm.

At a Reynolds number of 315,000, noticeable effects of bluntness were observed over a range of spin rates from 750 to 1,500 rpm for both 8° and 10° angles of attack. This range is coincident with the location of the

74

maximum positive side force. Trends similar to those observed in the first phase at zero angle of attack were noted. For the non-spinning case at 10%, a negligible effect of bluntness for the low Reynolds number case was observed. There was little difference between the 8° and 10° sequences at a particular spin rate. Figures 48a, b, c and d display effects of increasing bluntness at a Reynolds number of 315,000 and spin rate of 750 rpm at 10°. The effects of the sharp nose and 10% bluntness ratio nose appear to be identical to those of the 20% and 30% noses, although Figures 48a and b show a boundary layer transition region which is further downstream. The low frequency waves moved upstream and were first visible at a point 2 calibers behind the tip for the 20% nose, as compared to just in front of the nose/mid-section juncture for the first two cases. Also, a greater portion of the mid-section seemed to be turbulent. The above trend continued for the 30% nose, where the waves appeared just slightly further upstream than those on the 20% nose. Furthermore, the turbulent region growing along the mid-section was slightly larger in area.

Figures 49a, b, c and d for the low Reynolds number case, and 1,250 rpm at 8°, do not exhibit the same trends in the boundary layer development as in Figure 48. On the 10% nosed model, the waves appeared further downstream than on the sharp-nosed model and first became visible where the nose and mid-section join. Also, striation breakdown into turbulence did not occur until the boattail of the 10% nose. On the 20% nosed model, the waves first appeared upstream at the same location on the nose as they did on the sharp-nosed model. However, the waves seemed to be wider and of a lower frequency than for either of the previous two noses, and a greater portion of the mid-section region is turbulent. Similar low frequency waves appeared on the 30% nose at about the same location as those on the 20% nose, but the turbulent region on the mid-section had decreased slightly in area.

Figures 50a, b, c and d display the effects of bluntness at the low Reynolds number and 10° angle of attack for a spin rate of 1,500 rpm. The waves developed at about the same location for the sharp nose and the 10% nose, with the 10% nose showing a larger turbulent region along the mid-section. Further increases in bluntness caused a substantial upstream movement of the location of the appearance of the waves for the 20% and 30% noses. In addition, a secondary instability occurred in the first two or three waves
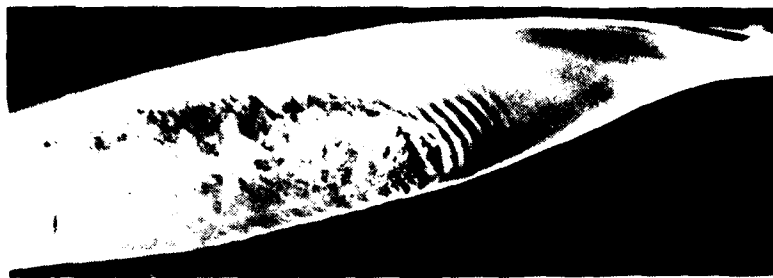
a)   Sharp Secant Ogive Nose

b)   10% Bluntness Ratio Nose
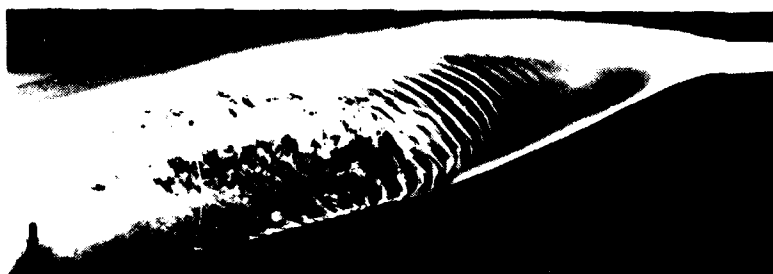
c)   20% Bluntness Ratio Nose

d)   30% Bluntness Ratio Nose

Fig. 48.   Smoke Visualization of Bluntness Effect at a
Camera Axis 55° from the Flow Direction Facing Upstream for:
R_L (Sharp Nose) = 315,000, 750 rpm, V/U_∞= 0.48, ι = 10°.
(Starboard View)

a) Sharp Secant Ogive Nose

b) 10% Bluntness Ratio Nose

c) 20% Bluntness Ratio Nose

d) 30% Bluntness Ratio Nose

Fig. 49 . Smoke Visualization of Bluntness Effect at a
Camera Axis 55° from the Flow Direction Facing Upstream for:
R_L (Sharp Nose) = 315,000, 1250 rpm, V/U_∞ = 0.824, α = 8°.
(Starboard View)

a) Sharp Secant Ogive Nose

b) 10% Bluntness Ratio Nose

c) 20% Bluntness Ratio Nose

d) 30% Bluntness Ratio Nose

Fig. 50 . Smoke Visualization of Bluntness Effect at a
Camera Axis 55° from the Flow Direction Facing Upstream for:
R_L (Sharp Nose)= 315,000, 1500 rpm, W/U_∞= 1.02, α = 10°.
(Starboard View)

upstream of the nose/mid-body juncture, yielding an earlier transition to turbulence. The mid-section turbulent region was similar for the 20% and 30% cases and was larger than that for the 10% case.

The effect of bluntness on boundary layer development was not limited to the low Reynolds number case. Figures 51a, b, c and d display transition at a Reynolds number of 1,030,000 at an angle of attack of 10° and a velocity ratio of 0.546. Comparison of the sharp nose and 10% bluntness ratio nose showed a marked difference in the location of the wave formation. Waves were visible over about one-third of the sharp nose near the mid-section. For the 10% nose, waves formed much earlier on the nose at about 1 caliber from the nose tip and appeared to cover more than one-half the 10% starboard surface. The turbulent region was larger than on the sharp nose, such that it almost completely covered the mid-section of the 10% nose. The boundary layer development on the 20% bluntness ratio model appeared to be similar to that of the 10% nose, with the exception that lower frequency waves appeared near the mid-section/nose juncture of the 20% nose. These waves seemed to increase in frequency for the 30% nose and became turbulent over the entire mid-section surface.

SUMMARY OF EXPERIMENTAL RESULTS

Non-Spinning Baseline Model at Zero Angle of Attack

The high speed smoke photographs and pressure data indicate several trends which occur as Reynolds number is varied during the study of transition at zero free stream pressure gradient.

The smoke photographs show that the separation point moves up the boattail as Reynolds number is increased. The separation point on the boattail was found to occur when the pressure coefficient was about (-0.015) for all the non-spinning, zero angle of attack cases studied. At the separation point, vortex rings or "doughnuts" are formed and accelerate rapidly with the flow. These rings become turbulent more quickly as Reynolds number is increased.

Two-dimensional, i.e., axisymmetrical, Tollmien-Schlichting waves appeared sporadically along the body at R_L = 631,000 and appeared continuously at all higher Reynolds numbers. Trusses were formed on the body for Reynolds
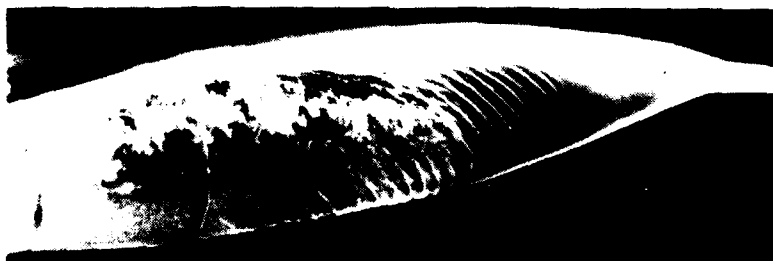
79

a) Sharp Secant Ogive Nose
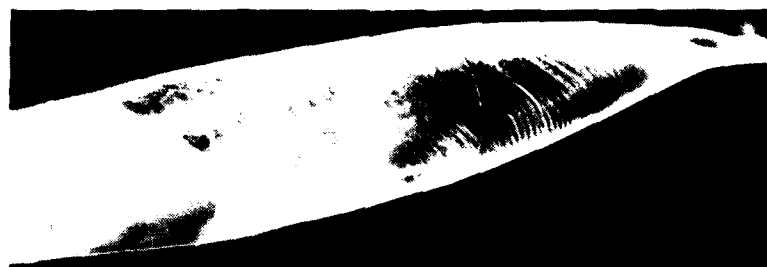
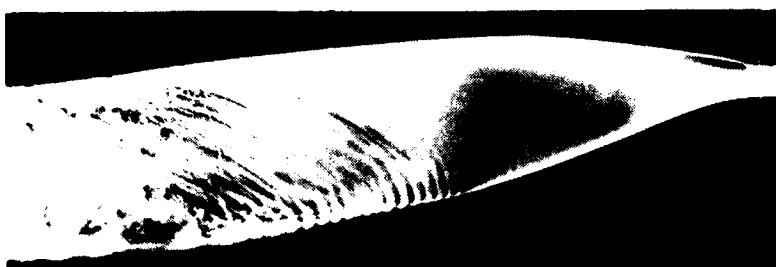b) 10% Bluntness Ratio Nose

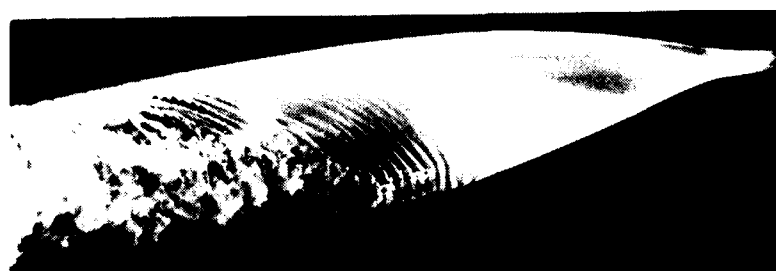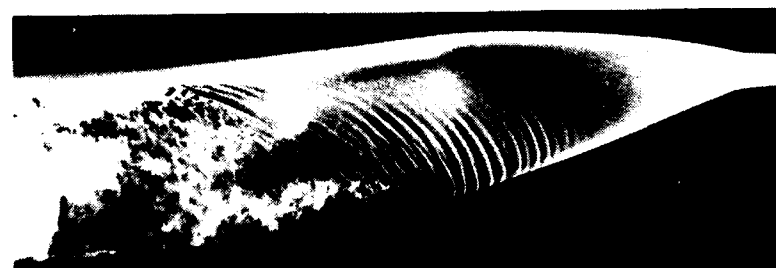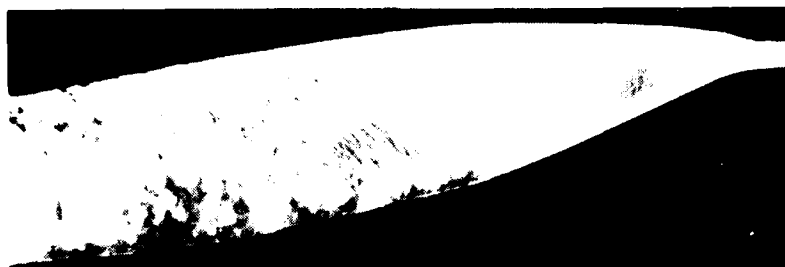c) 20% Bluntness Ratio Nose
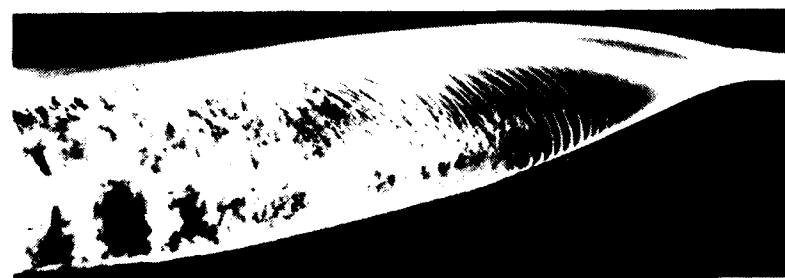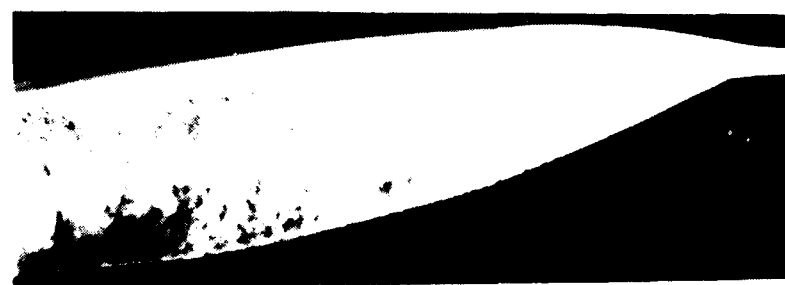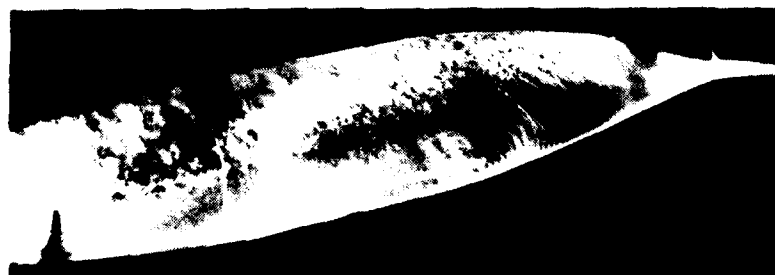

d) 30% Bluntness Ratio Nose

Fig. 51. Smoke Visualization of Bluntness Effect at a
Camera Axis 55° from the Flow Direction Facing Upstream for:
R_L (Sharp Nose) = 1,030,000, 2500 rpm, V/U_∞= 0.546, ι = 10°.
(Starboard View)

30

numbers 928,000 and 1,030,000. At the highest Reynolds number, there was continuous formation of the two-dimensional waves.

Three-dimensional deformation of the two-dimensional waves into trusses occurred sporadically for Reynolds numbers equalling 928,000, and almost continuously for R_L = 1,030,000. At no time was the transition process entirely washed off the body, as observed by Brown[27] and his colleagues on the tangent ogive models.

Spinning Baseline Model at Zero Angle of Attack

The smoke visualization of the spinning model at zero angle of attack showed the following effects as spin rate was increased.

A second transition process, the formation of striations in the smoke (a manifestation of vortices originating near the model nose), occurred when the velocity ratio was greater than $V/U_\infty \approx 0.4$. When the velocity ratio was less than 0.4, only a skewness in the tips of the trusses could be observed when trusses were present. The formation of striations was primarily dependent upon the non-dimensional velocity ratio, V/U_∞, and relatively independent of Reynolds number over the range used. The striations usually originated near the nose close to the surface of the model. The entire transition process took place over a slightly shorter region when the Reynolds number was increased. The striations broke down in the form of beads or knots, somewhat resembling a tightly twisted rope. The boundary layer along the mid-section of the model was entirely turbulent for values of V/U_∞ greater than 1.0.

Spinning Baseline Model at Angle of Attack

The photographic data, together with the force data, suggest that the net Magnus lift is a result of a combination of effects. A negative Magnus force can result from the following mechanism. If the angle of attack were large enough to yield significant cross-flow ($\geq 4°$), an asymmetric transition region would form on the side of the model where the cross-flow opposes the direction of the rotation of the model. This was illustrated dramatically in the photographs of the 4°, 6° and 10° angles of attack. A higher spin rate was required to move the elliptical transition region on the starboard side of the model as the angle of attack and, therefore, the cross-flow velocity, was increased.

A positive Magnus force was generated only at relatively high spin rates

81

and angles of attack. The spin and angle of attack result in a circulation being imposed on the potential flow field surrounding the model, resulting in the classical Magnus lift. As the angle of attack was increased, the positive Magnus effect became a stronger function of spin rate. However, it can be inferred that the positive Magnus lift is small at low spin rates. Also, it can be assumed that the net lift on the model results from the superposition of the negative and positive lifting mechanisms present at a particular spin rate and angle of attack.

Influence of Nose Bluntness - Non-Spinning Model at Zero Angle of Attack

From the smoke visualization photographs, the affect of bluntness appeared to be negligible for the lower Reynolds number case. For Reynolds numbers of 928,000 and 1,030,000, however, increasing bluntness from sharp to 10% nose and again from 10% to 20% nose seemed to result in earlier development of boundary layer transition phenomena. This was evidenced in the upstream movement with increasing bluntness of the initial Tollmien-Schlichting wave vortex loop development and subsequent breakdown to turbulence. Interestingly enough, further increases in bluntness in going to the 30% bluntness ratio nose seemed to result in a slight downstream movement of the above phenomena.

Spinning Model at Zero Angle of Attack

Similar trends in the flow visualization data were observed at zero angle of attack when the model was spinning. Once again, only at the higher Reynolds numbers were bluntness effects noted in the observation of earlier development of boundary layer transition phenomena. In going from the sharp to 10% bluntness ratio nose, striation formation seemed to occur earlier on the mid-section of the 10% nose. The increase in bluntness from 10% to 20% was particularly effective as, in every sequence, transition phenomena seemed to develop earlier or formed further upstream on the model. This affect of bluntness trend was manifested in the location of the two-dimensiona. Tollmien-Schlichting wave formation, transition to three-dimensional truss or vortex loop, and subsequent breakdown to turbulence as well as the location of the formation of cross-flow induced vortices o, striations and their transition to turbulence. In addition, some sequences showed an increase

82

in striation frequency. The 20% and 30% nose bluntness increase did not effect nearly as consistent a change in the boundary layer formation. In some cases, the additional nose bluntness caused a continued forward movement of the turbulent transition region near the rear of the model, whereas, in the others, the bluntness-affected movement of the striation location changed direction and moved rearward with the increasing bluntness, similar to the non-spinning case. In still other sequences, the transition phenomena on the 30% nose appeared to be similar in location and description to the 20% nose.

Spinning and Non-Spinning Model at Angle of Attack

Bluntness sequences of smoke visualization photographs show negligible affects of bluntness for the zero spin case at 10° angle of attack for a Reynolds number of 315,000.

The Magnus force measurements made at the low Reynolds number case of 315,000 were not conclusive as to the effect of nose bluntness since the forces generated were so small (as low as $\simeq 0.01$ Newton), and differences in the magnitude of the measured side force coefficients were within the range of experimental error. However, the nature and patterns of the data for each nose were consistent and very similar, and the trends in the curves were supported by the visualization data. It is hoped that the recent completion of a more sensitive and stable strain gauge amplifier will yield more conclusive information for the low Reynolds number case in the near future.

Since the side forces generated at the high Reynolds number, 1,030,000, were approximately twice those of the corresponding low Reynolds number test, more accurate measurements with better resolution enabled more conclusive data. For 4° angle of attack at a Reynolds number of 1,030,000, the data for all noses was clustered around the zero C_y axis throughout the spin rate range. All curves showed a gradual increase in C_y up to a maximum value of about 0.025 at a velocity ratio of 0.50, and then leveled off along the zero C_y axis. Increasing the angle of attack tended to displace the indi.idual curves with respect to the C_y axis or, in other words, the affect of nose bluntness appeared to increase with increasing angle of attack. This is verified by the smoke visualization data. At 6° angle of attack, Magnus

force increased with each increase in nose bluntness, particularly in the asymmetric transition region area, up to a velocity ratio of about 0.65. At higher velocity ratios where Magnus force increased linearly with increasing spin rate, the above relationship is not nearly so accurate. At 8° and 10°, once again, the more blunt noses seemed to develop larger Magnus forces for velocity ratio values in the asymmetric transition region. For 8° angle of attack, the 20% and 30% bluntness ratio noses appeared to be grouped together, as were the sharp and 10% bluntness ratio noses. At 10° angle of attack, the 20% nose was measured to have the maximum Magnus force or most negative C_y value throughout the asymmetric transition region range. As suggested by the side force data and verified by the smoke visualization sequences, the affect of varying nose bluntness was greatest and most consistent in the spin rate range of the asymmetric transition region. For the low Reynolds number tests, this corresponded to a spin rate range from about 300 rpm to approximately 1,750 rpm or velocity ratios from 0.18 to 1.20. For a Reynolds number of 1,030,000, asymmetries in the boundary layer were observed from about 750 rpm to 3,500 rpm for a comparable velocity ratio range to the low Reynolds number case. The ranges defined above include flow asymmetries throughout the angle of attack range of this investigation. Flow asymmetry observations at any particular angle of attack were made in a somewhat narrower range.

The flow visualization sequences at angle of attack exhibit similar trends to the zero angle of attack observations. In most cases, increasing bluntness produced an earlier boundary layer transition manifested in an upstream movement of the low frequency wave formation or an increased turbulent area generally found on the model mid-section. In addition, increased bluntness caused what appeared to be a frequency change in the low frequency disturbances that somewhat resembled the Tollmien-Schlichting waves from the zero angle of attack investigation. However, the effect could either result in an increased or decreased frequency of the waves; no trend was apparent. The sharp nose to 10% bluntness ratio comparison was inconsistent in that the transition phenomena sometimes moved upstream and, in other cases, downstream with increasing bluntness. The 10% to 20% increase in bluntness ratio, once again, seemed to be particularly effective in producing a forward movement of the boundary layer transition phenomena.

This was easily the most consistent trend observed in the flow visualization studies. The 20% to 30% increase in nose bluntness generally resulted in little or no movement of the initial boundary layer instabilities, with occasional exceptions. However, in some cases, the increase effected a change in frequency of the low frequency waves or a change in the total area of the turbulent region. In most comparisons, the smoke-visualized boundary layer of the 30% bluntness ratio nose reasonably resembled that of the 20% nose.

CONCLUSIONS

This investigation brings to mind a major short-coming in the theories which attempt to model the boundary layer and Magnus characteristics of spinning bodies at small angles of attack. The flow visualization indicates the transition process occurs symmetrically about the axis of revolution for $\alpha = 2°$. Theoretical models have included mixed laminar/turbulent boundary layers, but to no avail. The Magnus forces predicted by such theories[1] are always positive with respect to angle of attack and spin rate, similar to what was observed at relatively high spin rates in this investigation. However, unless the full three-dimensional transition process is considered, the flow field will not be correctly modeled and force predictions will be inaccurate.

This experimental effort has illustrated several boundary layer developments which suggest possible mechanisms for generating a Magnus lift. Although hot-wire studies of the flow field surrounding the model were not conducted, several fundamental laws of fluid mechanics reinforce the conclusion that the cross-flow instability influences the cross-flow velocity. The negative Magnus force is due to a lower average pressure on the starboard side than on the port side of the model. This difference in pressure must correspond to a difference in the average velocity across the two sides of the model; the average velocity must be greater across the starboard side. Finally, the different average velocities must be related to developments in the boundary layer, and the asymmetric transition region is the serious difference between the boundary layers on the starboard and port sides of the model.

The affect of nose bluntness on the side force found in this study

appears to be consistent with earlier work. The bluntness had a greater affect on the side force at the higher Reynolds number. The most noticeable effects of nose bluntness were changes in the asymmetric transition region, which correlated well with the "bump" in the side force data.

For particular combinations of free stream velocity and spin rate, the variations of nose bluntness appear to affect the development of the boundary layer. The effect is generally manifested in the position or location of the appearance of Tollmien-Schlichting waves or cross-flow vortices. Transition phenomena typically appear further upstream on the 20% nosed model. A change from 10% to 20% nose bluntness seems to be particularly effective. Comparisons between the 20% and 30% noses or between the sharp and 10% noses show no consistent or significant change in the location of the transition region.

The study of the simultaneous occurrence of Tollmien-Schlichting waves and the spiraling vortices is continuing. The simultaneous occurrence of the Tollmien-Schlichting waves and cross-flow vortices discovered in an earlier study[28] with the sharp nose also occurred with blunt noses.

The data obtained will be compared with other experimental and analytical investigations. It is hoped these data will aid in the development of improved computational models.

1.0

4.5
2.8
2.5
3.2
2.2
3.6
4.0
2.0
1.8

1.1

1.25   1.4   1.6
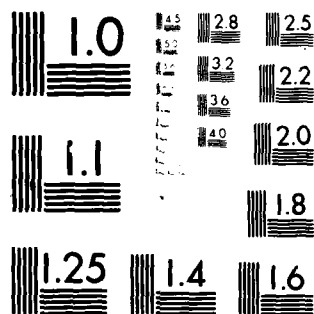
MICROCOPY RESOLUTION TEST CHART
NATIONAL BUREAU OF STANDARDS 1963 A

REFERENCES

[1]Vaughn, H.R., and Reis, G.E., "A Magnus Theory for Bodies of Revolution," Sandia Laboratories Report, SC-RR-720537, January 1973.

[2]Lin, T.C., and Rubin, S.C., "Viscous Flow over Spinning Cones at Angle of Attack," AIAA Journal, Vol. 12, No. 7, pp. 965-974, July 1977.

[3]Dwyer, H.A., and Sanders, B.R., "Magnus Forces on Spinning Supersonic Cones - Part I: The Boundary Layer," AIAA Journal, Vol. 14, No. 4, pp. 498-504, April 1976.

[4]Sanders, B.R., and Dwyer, H.A., "Magnus Forces on Spinning Supersonic Cones - Part II: Inviscid Flow," AIAA Journal, Vol. 14, No. 5, pp. 576-582, May 1976.

[5]Graff, G.Y., and Moore, F.G., "The Effect of Boattail Shape on Magnus," NSWC/DL TR-3581, December 1976.

[6]Morton, J.B., Jacobson, I.D., and Sanders, S., "Experimental Investigation of the Boundary Layer on a Rotating Cylinder," University of Virginia, Report No. SS-3318-112-74, May 1974.

[7]Sturek, W.B., "Boundary Layer Studies on a Spinning Tangent-Ogive Cylinder Model," BRL Report No. 1801, July 1975.

[8]Sturek, W.B., Dwyer, H.A., Kayser, L.D., Nietubicz, C.J., and Reklis, R.P., "Computations of Turbulent Boundary Layer Development over a Yawed, Spinning Body of Revolution with Application to the Magnus Effect," BRL Report No.1985, May 1977; also published in Proceedings of Symposium on Turbulent Shear Flows, Pennsylvania State University, April 18-20, 1977.

[9]Kayser, L.D., and Sturek, W.B., "Experimental Measurements in the Turbulent Boundary Layer of a Yawed, Spinning Ogive-Cylinder Body of Revolution at Mach 3.0 - Part II; Data Tabulation," ARBRL-MR-02813, March 1978.

[10]Kayser, L.D., and Sturek, W.B., "Turbulent Boundary Layer Measurements on the Boattail Section of a Yawed, Spinning Projectile Shape at Mach 3.0," ARBRL-MR-02880, November 1978.

[11]Sturek, W.B., "Boundary Layer Studies on a Spinning Cone," BRL-R-1649, AD 762564.

[12]Kegelman, J.T., Nelson, R.C., and Mueller, T.J., "Boundary Layer and Side Force Characteristics of a Spinning Axisymmetric Body," AIAA Paper No. 80-1584, August 1980.

[13]Nietubicz, C.J., and Opalka, K., "Supersonic Wind Tunnel Measurements of Static and Magnus Aerodynamic Coefficients for Projectile Shapes with Tangent and Secant Ogive Noses," ARBRL-MT-02991, February 1980.

[14]Martin, J.M., "An Experimental Correlation between the Flow and Magnus Characteristics of a Spinning Ogive Nose Cylinder," Ph.D. dissertation, University of Notre Dame, August 1971.

[15]Sturek, W.B., et al., "Computations of Magnus Effects for a Yawed, Spinning Body of Revolution," AIAA Journal, Vol. 16, No. 7, pp. 687-692, July 1978.

[16]Sturek, W.B., Mylin, D.C., and Bush, C.C., "Computational Parameters Study of the Aerodynamics of Spinning Slender Bodies at Supersonic Speeds," AIAA Paper No. 80-1585, August 1980.

[17]Sturek, W.B., and Schiff, L.B., "Computations of the Magnus Effect for Slender Bodies in Supersonic Flow," AIAA Paper No. 80-1586, August 1980.

[18]Acharya, M., "Effects of Compressibility of Boundary Layer Turbulence," AIAA Journal, Vol. 15, No. 3, pp. 303-304, March 1977.

[19]Morkovin, M.W., "On the Many Faces of Transition," Viscous Drag Reduction, C.S. Wells, editor, Plenum Press, New York, pp. 1-31, 1969.

[20]Landahl, M.T., "Wave Breakdown and Turbulence," Proceedings of International Symposium on Modern Developments in Fluid Dynamics, SIAM, pp. 215-236, 1977.

[21]Betchov, R., Transition: Handbook of Turbulence, Vol. 1, W. Frost and T.H. Moulden, editors, Plenum Publishing Corp., pp. 147-164, 1977.

[22]AGARD-CP-224, "Laminar-Turbulent Transition," Proceedings of AGARD Fluid Dynamics Panel Symposium, Copenhagen, Denmark, 1977.

[23]Morkovin, M.W., "Technical Evaluation Report of the Fluid Dynamics Panel Symposium on Laminar-Turbulent Transition," AGARD-AR-122, June 1978.

[24]Swinney, H.L., and Gollub, J.P., "The Transition to Turbulence," Physics Today, pp. 41-49, August 1978.

[25]Cebeci, T., and Bradshaw, P., Momentum Transfer in Boundary Layers, Hemisphere Publishing Corp., 1977.

[26]Eppler, R., and Fasel, H. (editors), "Laminar-Turbulent Transition," IUTAM Symposium, Stuttgart, Germany, 1979.

[27]Brown, F.N.M., "The Physical Model of Boundary Layer Transition," Proceedings of Ninth Mid-Western Mechanics Conference, University of Wisconsin, pp. 421-429, August 1965.

[28]Mueller, T.J., Nelson, R.C., Kegelman, J.T., and Morkovin, M.V., "Smoke Visualization of Boundary Layer Transition on a Spinning Body," to be published in AIAA Journal, December 1981.

[29]Mueller, T.J., "On the Historical Development of Apparatus and Techniques for Smoke Visualization of Subsonic and Supersonic Flows," AIAA Paper No. 80-0420-CP, March 1980.

[30]Gregory, N., Stuart, J.T., and Walker, W.S., "On the Stability of Three-Dimensional Boundary Layers with Application to the Flow Due to a Rotating Disk," Phil. Trans., Royal Society (London), Series A, Vol. 248, No. 943, pp. 155-199, July 1955.

[31]Poll, D.I.A., "Three-Dimensional Boundary Layer Transition via the Mechanisms of 'Attachment Line Contamination' and 'Cross-Flow Instability'," published in IUTAM Symposium, Laminar-Turbulent Transition, R. Eppler and H. Fasel, editors, Stuttgart, Germany, 1979.

[32]Poyston, J.P., and Brown, F.N.M., "An Associated Force and Flow Study of a Tangent Ogive Nosed Cylinder," limited publication and distribution by Bureau of Naval Weapons, 1959.

[33]Zehentner, R.J., Nelson, R.C., and Mueller, T.J., "A Visual Study of the Influence of Nose Bluntness on the Boundary Layer Characteristics of a Spinning Axisymmetric Body," AIAA Paper No. 81-1901, August 1981.

[34]Covert, E.E., and Eberhardt, D.S., "A Vortex Model for Magnus Forces at Low Speeds, Spins and Angles," submitted to publication in AIAA Journal, February 1981.

[35]Zehentner, R.J., "An Experimental Investigation of the Influence of Nose Bluntness on the Boundary Layer and Side Force Characteristics of Spinning Axisymmetric Bodies," M.S. thesis, University of Notre Dame (in preparation), December 1981.